Cryogenic Selective Surfaces

NIAC Phase II Study
Final Report

September 2018

Robert C. Youngquist, Ph.D.
Mark A. Nurge, Ph.D.
Wesley L. Johnson
Tracy L. Gibson, Ph.D.

i.   Executive Summary

There are many challenges involved in deep-space exploration, but several of these can be mitigated, or even solved, by the development of a coating that reflects most of the Sun's energy, yet still provides far-infrared heat emission. Such a coating would allow non-heat-generating objects in space to reach cryogenic temperatures without using an active cooling system. This would benefit deep-space sensors that require low temperatures, such as the James Webb Telescope focal plane array. It would also allow the use of superconductors in deep space, which could lead to magnetic energy storage rings, lossless power delivery, or perhaps a large-volume magnetic shield against galactic cosmic radiation. However, perhaps the most significant enablement achieved from such a coating would be the long-term, deep space storage of cryogenic liquids, such as liquid oxygen (LOX).

In our Phase I NIAC study, we realized that a combination of scattering particles and a silver backing could yield a highly effective, very broadband, reflector that could potentially reflect more than 99.9% of the Sun's irradiant power. We developed a sophisticated model of this reflector and theoretically showed that cryogenic temperatures could be achieved in deep space at one astronomical unit (1 AU) from the Sun. We showed how this new reflector could minimize heat conduction into the cryogenic tanks by coating the tank support struts. We then modelled a strawman architecture for a mission to Mars, using a coated LOX tank, coated struts, and infrared shields, to show that with our new coating it would be possible to maintain liquid oxygen passively. As a result of this work a patent application was generated and a paper published in Optics Letters [7].

Our Phase II NIAC study had two primary goals, to develop a rigid version of the cryogenic selective surface proposed in Phase I and to test its performance in a simulated deep space environment. During the first year of the project the work concentrated on developing rigid tiles of BaF_2, leading to tiles as large as 4 inches in diameter that transmitted very little visible light. In addition, during the first year a simulated deep space environment was created using a vacuum chamber and cryocooler. Using this facility, we showed that our BaF_2 tiles absorbed less than ¼% of 375 nm radiation, a significant milestone for the work. During the second year of the project, we continued to develop the BaF_2 tiles and we put significant effort into the construction of a deep space environment where we could project simulated solar radiation onto a sample.

In the spring of 2018, we conducted our first solar simulator test with BaF_2 and saw about 3.6% absorption. This is better than the state-of-the-art, but disappointing since predictions were for much lower absorption. We, erroneously, attributed this absorption to water retention by the BaF_2, and decided to change materials. We considered several oxides and settled on yttrium oxide (Y_2O_3) for further development, because it is broadband, lightweight, has high index, and is hydrophobic. In July 2018 we conducted our first test of a rigid tile of Y_2O_3 in the simulated deep space environment and saw significant absorption again. We then realized that the issue was not water, but mid-wave radiation passing through the tile and being absorbed by the temperature sensor and the varnish used to hold it in place. We wrapped the sensor in silver foil, re-ran the test, and saw much lower absorption; only 1.1%. We then re-ran the BaF_2 tile and saw 1.4% absorption. These values are almost adequate to maintain LOX in deep space, but we suspect that there are still issues in our test apparatus; we suspect thermocouple wires may be absorbing radiation. Further, post-NIAC, testing will better determine the performance of our new solar reflector.

In order to restrict the size of this report, we will only briefly describe topics that we have previously published, allowing us to devote more time to new material. So minimal material will be devoted to modeling the material and deep space cryogenic storage, while longer sections will cover our material development, simulated deep space testing, and new applications. The Launch Service Program (LSP) requested that we explore ways to use this new coating to maintain LOX in low Earth Orbit and that work is described. In addition, the Nuclear Thermal Propulsion (NTP) Program asked us to explore ways to reduce the heat load for liquid hydrogen, resulting in the development of a spray-on version of the coating that should significantly improve in-space multi-layer insulation performance.

Contents

1. Background-Brief Summary of Phase I Results

Selective surfaces [1], also known as thermal control coatings, are often used in spacecraft applications to minimize the absorption of solar radiation, yet allow infrared (IR) energy to be emitted [2–4]. These coatings allow the emission of waste heat while minimizing the solar heat load, providing thermal control of spacecraft. The best currently available solar reflectors absorb 6% of the Sun's power in the 250 nm to 2500 nm range [5] and absorb additional Solar power at wavelengths longer than 2500 nm. Therefore, state-of-the-art solar reflectors likely absorb more than 100 W/m^2 of the Sun's irradiant power, while emitting roughly 400 W/m^2 when at 300 K. This allows a net energy loss providing cooling to a spacecraft, however if a plate were covered with this solar reflector and turned to face the Sun, it would come to an equilibrium temperature of about 200 K (assuming no heat flow out of the back of the plate). This is cold, but not cold enough to allow storage of cryogens or to operate superconductors.

The limitations of these state-of-the-art selective surfaces are two-fold; they absorb significant ultraviolet energy and significant long wave infrared energy. They are designed as second surface mirrors, with an outer layer of fused silica and a layer of silver on the backside. The Sun's ultraviolet and visible energy goes through the fused silica and hits the silver, where the visible energy is reflected back through the glass, but much of the ultraviolet is absorbed. The fused silica transmits poorly beyond 4 microns and absorbed most of the Sun's power at wavelengths longer than that.

During our Phase I activity [6] we realized that the way to make a better solar reflector, one that could yield cryogenic temperatures in deep space, was to cover a thin layer of silver with a layer of scattering particles. The particles should be composed of a broadband material that has minimal absorption between 210 nm and 10 microns (see Figure 1-1 for the Sun's spectrum), and their size should be roughly 150 nm in diameter so that they have a peak Mie scattering at 480 nm to match the Sun's peak emission. Figure 1-2 shows the concept more clearly. When ultraviolet and visible radiation hits this particle layer it efficiently scatters the irradiant power and most of that energy eventually makes its way back to the front of the coating. This backscattering is reminiscent of how white paint works and is seen in such everyday items as cotton fiber, salt, and clouds. At near to middle wavelengths, the radiation does not scatter as efficiently; Rayleigh scattering predicts a falloff in scattering efficiency as 1/wavelength to the fourth power. So this radiation scatters more deeply in the particle layer and some of this radiation reaches the silver where it is reflected. Infrared radiation in the 5-10 micron range propagates through the scatterer and reflects off of the silver. Finally, long wave infrared, beyond the transmission range of the particle-based material, is absorbed, and, since good absorbers are also good emitters, thermal power can be emitted in this wavelength band. Since the Sun contains a very small far-IR component, the surface can emit more power in this spectral region than it absorbs from the Sun, providing cooling.

The net result of this combination of scattering layer and silver is a solar reflector that is predicted to reflect 99.9% of the Sun's energy, allowing cryogenic temperatures to be reached. We developed a sophisticated model describing the performance of this composite entity, which appears in our Phase 1 NIAC report [6] and our Optics Letter [7]. Some of these concepts are not new. In 1961 Hibbard stated that cryogenic temperatures could be reached if an ideal selective surface could be fabricated, i.e. one that was perfectly reflecting below a cutoff wavelength and perfectly emitting above this wavelength [8]. And, in 1968 the optics community realized that a sufficiently thick layer of pressed particles could be used to achieve a nearly perfect reflector [9]. In our work we rediscovered both of these results (subsequently finding them in the literature), recognizing that by placing a metallic reflector (e.g. silver) behind the particle scattering layer that a nearly ideal selective surface could be fabricated.
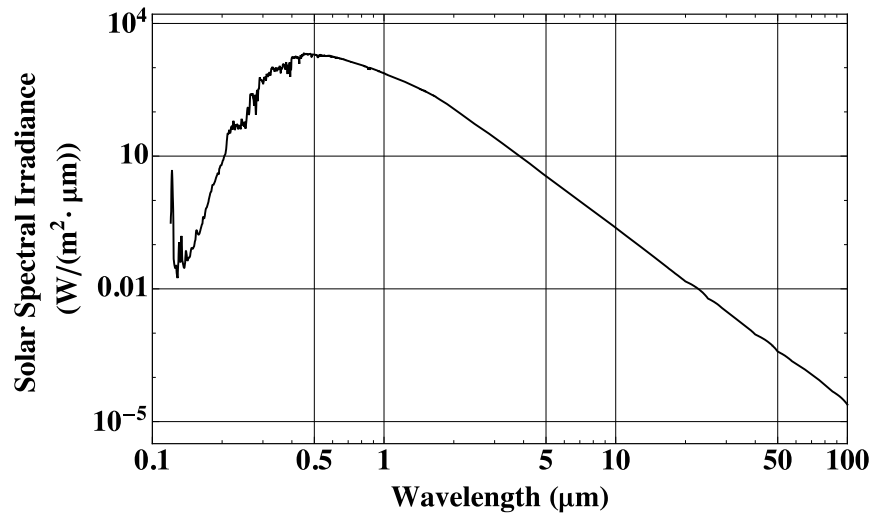
Figure 1-1. The deep space solar irradiance spectrum showing the variation in solar power density versus wavelength.
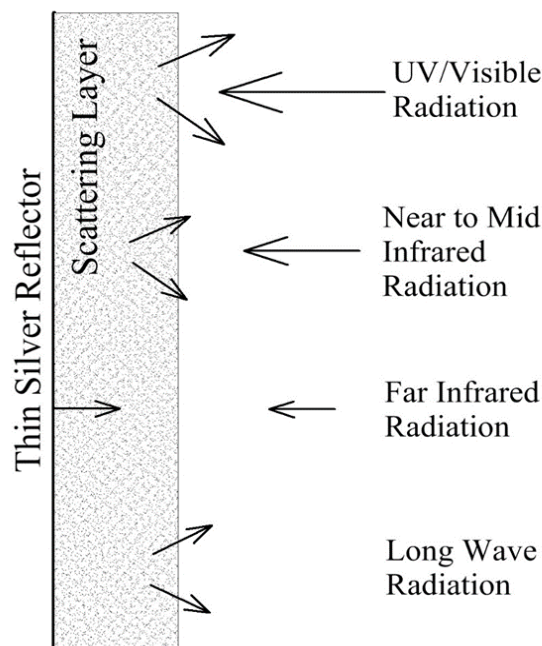

Figure 1-2. Our new cryogenic selective surface is composed of a particle scattering layer on top of a metallic film, such as silver. Ultraviolet and visible radiation is efficiently back scattered by the particles, mid-wave infrared is partially back scattered and partially reflected by the silver, far infrared is reflected by the silver, and the long wave radiation is absorbed, but also emitted.

During our Phase I effort we examined multiple broadband materials and calculated predicted temperatures for various thicknesses of these materials as powders on silver, coating spheres, cylinders, and plates. Figure 1-3 shows the predictions for these materials when a 5 mm thick layer coats a sphere. Each material is plotted versus its long wave

cut-off, i.e. the wavelength where it roughly transitions from transmitting to absorbing. The continuous plot is the predicted temperature for an ideal selective surface (i.e. a Hibbard surface) showing the theoretical minimum temperature that can be reached.
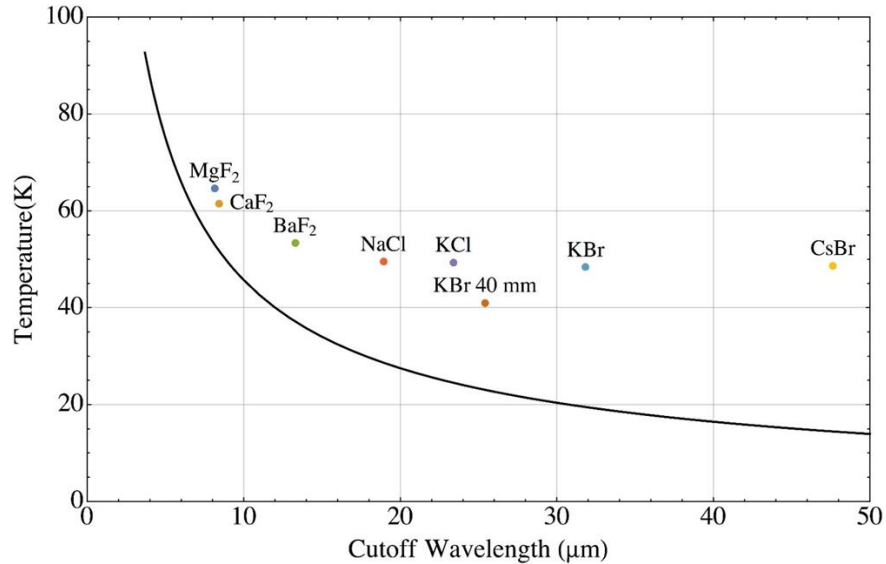

Figure 1-3. Predicted temperatures for 5 mm thick layers, of various broadband materials, covering a sphere compared to the theoretical limit. Seven materials are shown; MgF₂, CaF₂, BaF₂, NaCl, KCl, KBr, and CsBr, that achieve temperatures below 70 K.

These promising results led to co-funding and the award of a Phase II NIAC, the primary goals of which were to demonstrate a rigid version of our new coating and to verify its performance. The next two sections present the work performed to address these goals. Then, section 4 will present two applications analyzed for potential in-space use of this new coating.

While working the Phase II project we were awarded a second Phase I NIAC to develop our new coating into a highly efficient solar reflector that could potentially be used, not to achieve cryogenic temperatures, but to approach the Sun. This project, titled "Solar Surfing", required the construction of large rigid tiles for proposed testing at the Johns Hopkins Applied Physics Laboratory, and as such impacted the Phase II NIAC work. Some of those impacts are mentioned in this report, but details will not be repeated here that have already been documented in the Phase I final report for that project [10].

During the Phase II NIAC work we published a paper describing some of the work performed during the Phase I project and some from the first year of the Phase II effort [11]. Some of the material in that publication is repeated below, but not all.

2. Rigid Tile/Material Development and Analysis

The most important accomplishment of this Phase 2 NIAC project was the development of rigid versions of our new cryogenic selective surface. This section of the report reviews the work performed on that effort, however substantial details are omitted for space reasons and may be published in a later document. During most of the project Barium Fluoride (BaF_2) was the material of choice due to its broad transmission range and its relative insolubility (as compared to the other fluorides and various salts). Barium Fluoride is a well-known optical material that can be purchased as a high purity powder (Sigma-Aldrich). As the project evolved and we went public with our work, Sigma-Aldrich was not able to supply BaF_2 powder in a timely fashion, so we synthesized our own powder using barium nitrate and ammonium fluoride by a method described in an earlier publication [10]. Doing this provided control of the particle size, allowing the reflectance spectrum to better match the peak of the Sun's emission (around 480 nm).

Later in the project, various issues with BaF_2 led us to consider other materials. Potassium Bromide (KBr) was studied, due to its very long wave transmission band, potentially allowing coated objects to come nearer to infrared emitters such as the Earth. Potential water absorption issues concerned us, so we spent most of the final eight months of the project studying and developing oxide-based cryogenic selective surfaces. These oxides, hafnium oxide (HfO_2), yttrium oxide (Y_2O_3), and zirconium oxide (ZrO_2) are hydrophobic, readily available (though purity was an issue), and have high indices of refraction indicating that they will scatter light well. However, their optical properties are not well known and additional analysis was necessary to determine if their absorption of solar radiation was low enough to reach cryogenic temperatures.

As we entered the end of the project, we began to consider composite materials. The oxides have high melting points and it was difficult to sinter them to form rigid tiles. So we mixed BaF_2 or KBr with the oxides and then heated the mixture near the melting point of the fluoride, so it could cool to a solid and hold the oxide particles in place. This approach had limited success, but led to second approach where we utilized the high water solubility of KBr. By dissolving KBr in water and then adding oxide particles (usually Y_2O_3) to the mixture, a white slurry, or paint, could be made. Applying this to a surface and letting it dry, caused the KBr to come out of solution and form a solid that held the yttrium oxide particles in place. The Nuclear Thermal Propulsion Program funded us to consider the use of our cryogenic selective surfaces to enhance the ability of maintaining liquid hydrogen (LH_2) on a trip to Mars. We have shown that by spraying this KBr/Y_2O_3 paint onto multi-layer insulation that we can lower the solar absorption and reduce the heat load on the LH_2 tanks. This topic is presented in section 4.3.

The discussion below concentrates first on material development, describing approaches and results for the fabrication of rigid tiles composed of various materials. After that, analysis of the tiles and materials is provided, concentrating on optical property measurements such as spectral reflectance and Fourier Transform Spectroscopy. Scanning electron microscope (SEM) images provide the particle sizes after sintering, which help explain some of the optical reflectance measurements. Material properties such as breakage strength and machinability close out the section.

2.1 Barium Fluoride (BaF_2)

2.1.1 Powder Samples

All of the materials considered for use as cryogenic selective surfaces were purchased or manufactured as powders/particles. To evaluate the optical properties of these powders they were packaged in 1-inch diameter holders as shown in Figure 2.1.1-1. The powders were sandwiched between windows composed of BaF_2, KBr, Sapphire, or B270 glass, allowing light to be directed through the powder or scattered off it. Typically, the thickness of the powder samples were either 3mm or 6mm thick, which was often sufficient to prevent nearly all visible light from propagating through the powder.

Figure 2.1.1-1. Typical powder test samples consist of a 1-inch diameter cylindrical holder, allowing two windows to sandwich the powder. This assembly permits reflectance and transmission measurements of the powder.

2.1.2   Rigid Tile Construction

In order to convert the loose particles into a rigid material, it was necessary to heat the powder to a temperature where the particles would merge at their contact points, but not melt, i.e. sinter. Initial experiments were conducted to determine the optimum sintering temperature for 3.5 grams of barium fluoride powder placed on a 3 mm thick, 1-inch diameter, barium fluoride window as a base substrate. Sintering was conducted in a Carbolite CWF 1300 Box Furnace equipped with an exhaust vent. Five different sintering temperatures were evaluated and the results are shown in Table 2.1.2-1. After choosing 780 °C as a best sintering temperature, multiple temperature profiles were explored resulting in the optimized sintering temperature profile shown in Table 2.1.2-2. Barium fluoride has a strong affinity for water [10] and one goal of the temperature profile was to ensure the removal of water before sintering started. Figure 2.1.2-1 shows a typical sintering result.

Table 2.1.2-1. Sintering temperatures evaluated for barium fluoride. 750 °C was not hot enough, 1000 °C caused too much melting, and 780 °C turned out to be best.

Temperature (°C)	Comments
750	Powder partially sintered; not mechanically stable
760	Powder partially sintered; more mechanically stable than 750 °C but still not very stable
780	High degree of sintering; mechanical stability good; good retention of particle size
800	High degree of sintering with some melting; mechanical stability good; slight loss of particle size
1000	High degree of melting; temperature is too high

Table 2.1.2-2. Optimized sintering conditions for barium fluoride powder sintering and for low water content pressed powder mixtures.

Temperature Profile	Comment
Ramp up to 250 °C	Hold at 250 °C for 10 minutes
Ramp from 250 °C – 500 °C	Hold at 500 °C for 10 minutes
Ramp from 500 °C – 750 °C	Hold at 750 °C for 10 minutes
Ramp from 750 °C – 780 °C	Hold at 780 °C for 60 minutes
Power off Furnace	Allow to cool overnight

Figure 2.1.2-1.   Barium fluoride powder sintering example showing three images of barium fluoride powder spread on top of a one-inch diameter, barium fluoride window labelled "before sintering" and an image of sintered barium fluoride on a barium fluoride window labelled "after sintering".

The sintered powder samples had poor mechanical properties and tended to fall apart even though the particles had fused together. It was decided that more particle contacts were needed so two changes were made. First, the powder was compacted by low-pressure compression (i.e. hand-pressing) and second, water was added to the dry powder to act as a lubricant and improve the workability of the mixture. In these experiments, a known mass of barium fluoride was added to a weighing boat, the appropriate mass of deionized water was added, and the mixture stirred to remove any large lumps. The mixture was placed into a mold equipped with a support or base material, pressed, and then sintered.

Early experiments were conducted using a water content greater than 40% (wt/wt) but these experiments produced samples that were highly cracked, making them unusable. Follow-on experiments were conducted using a water content ranging from 19 – 29% (wt/wt). The goal of these experiments was to produce a coating that could be applied in a method similar to that used for concrete application. For these experiments, different base materials were evaluated, including sintered barium fluoride discs, fused glass windows, aluminum discs (Al-2219-T81), and silver coated mirrors. These experiments were more successful than those conducted using water content greater than 40%, however most of these experiments still produced rigid samples with a high degree of cracking (Figure 2.1.2-2). Also, in all the trials, the sintered sample did not stick to the support material, likely due to the difference in thermal expansion between barium fluoride and the support material. A summary of high-water content experiments is shown in Table 2.1.2-3.

Figure 2.1.2-2. An example of a sintered barium fluoride sample produced with water content between 19% and 29%. The resulting tile has gaps in its surface, resembling cracks, where the material separated during sintering.

Table 2.1.2-3. Summary of experiments conducted with a high-water content mixture.

| Temperature (°C)	Water Content (wt/wt%)	Support	Comments
780	19	Al-2219-T81	Does not spread easily; too viscous; need to add more water
780	24.6	Sintered BaF$_2$	Mixture spreads easily; better than 28%; severe cracking observed; did not stick to BaF$_2$
780	27.4	Al-2219-T81	Mixture spreads easily; severe cracking observed; aluminum support warped during sintering; did not stick to aluminum
780	28	Sintered BaF$_2$	Mixture spreads relatively easily; maybe still a little too viscous; minor cracking observed; did not stick to sintered BaF$_2$
780	28	Silver Mirror	Mixture spreads relatively easily; mirror cracked during sintering; severe cracking observed; did not stick to silver mirror
780	28.2	Al-2219-T81	Mixture spreads relatively easily; no cracking observed; aluminum support warped during sintering; did not stick to aluminum
780	28.3	Fused Glass Window	Mixture spreads relatively easily; severe cracking observed before sintering
780	43.1	BaF$_2$ Window	Slurry is not viscous enough to spread easily; too much water
780	50	BaF$_2$ Window	Requires "sealed" mold; no visible cracking observed; SEM revealed severe cracking on surface

Under low pressure, the resulting barium fluoride samples still showed cracking, so we moved to high-pressure compaction using a pellet or hydraulic press. This approach required less water (less than 15% wt/wt) and the resulting tiles were self-supporting so a base was no longer needed. The high-water content approach required a modified sintering temperature profile to dry out the material, but the reduced water content permitted the use of the same sintering temperature profile as used for the powder, Table 2.1.2-2.

An optimal water content for the high pressure compaction was found to be 10% (wt/wt). Early experiments were conducted using either a Specac Atlas Manual Hydraulic Press (Model GS15011) or an Across International Desktop Pellet Press (Model MP24A) and 32 mm diameter stainless steel molds, which were increased to 40 mm diameter for later experiments (Figure 2.1.2-3).

Figure 2.1.2-3. Specac 32 mm and 40 mm diameter steel molds and assorted dies or plungers used in a hydraulic press to compact the barium fluoride powder.

The face of the initial BaF_2 discs showed a brown blemish, observed after sintering, due to an interaction with the stainless steel die—this was likely a result of contamination of the die. This was alleviated by using an inert polymer barrier film placed between the powdered BaF_2 and the stainless steel dies prior to compression and removed before sintering. Figure 2.1.2-4 shows an example of a pre-sintered barium fluoride pressed disk. Increasing the applied force results in more particle-to-particle contacts and yields stronger material, but reduces the particle surface area and hence the scattering. So too little force yields a weak material and too much force yields a poor scatterer. Testing with different applied forces optimized the optical properties, yet maintained structural integrity.
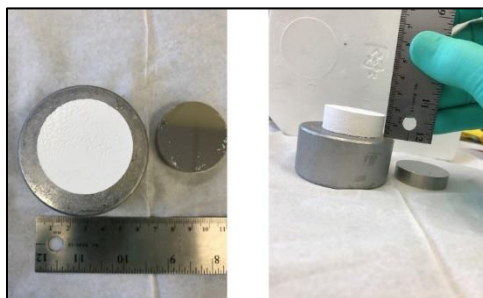
Figure 2.1.2-4. A top down and a side view of a pre-sintered BaF_2 disc, 40 mm x 14 mm, compressed with a pressure of 0.25 MPa.

The steel molds could not be placed in the oven, requiring the removal of the pressed powder sample from the mold before sintering. This often resulted in damage to the fragile, pre-sintered, pressed powders. To resolve this, we fabricated seven custom molds from high-temperature ceramic (Ultra-High-Temperature Alumina Ceramic, McMaster-Carr, Part Numbers 8978T67 and 8978T65). The molds were all two-part; composed of a form and a baseplate, as shown in Figure 2.1.2-5. Aluminum rams (see Figure 2.1.2-5) were fabricated for sample preparation and a Carver Press was used to apply pressure. The advantage of the ceramic molds is that the pressed powder can stay in the mold during the sintering process.

The first mold fabricated was a 2-inch square mold (Figure 2.1.2-5) and multiple samples were fabricated using this, with the best samples shown in Figure 2.1.2-6. The next ceramic mold fabricated was a 4-inch diameter circular mold and a sample was prepared using this (Figure 2.1.2-7). Then, a 4-inch square mold was fabricated and a test sample was prepared (Figure 2.1.2-7). Several smaller ceramic molds were fabricated to support sample preparation, including 0.8-inch diameter, 1.5-inch diameter, and 2.0-inch diameter circular molds. The 4-inch samples show that the fabrication process is scalable up to 4-inches, but these were the largest samples produced. Larger tiles may be possible, but there will be a limit. In all barium fluoride tests, the sintered tile is smaller than the mold, so for tiles up to four-inches, the shrinkage pulls the material in from the sides. We expect that at some size above four-inches the pressed powder will break up into smaller pieces as it shrinks in the oven.
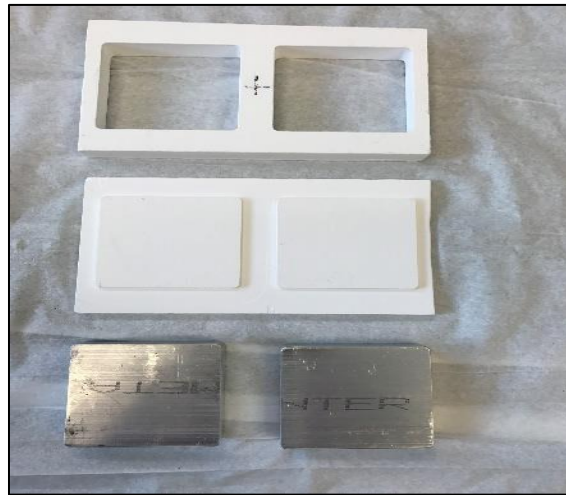

Figure 2.1.2-5. This is a 2-inch square alumina ceramic form and baseplate and two aluminum rams or pistons. The form is placed on the baseplate and powder placed into the form. Then the ram is used to compress the powder.
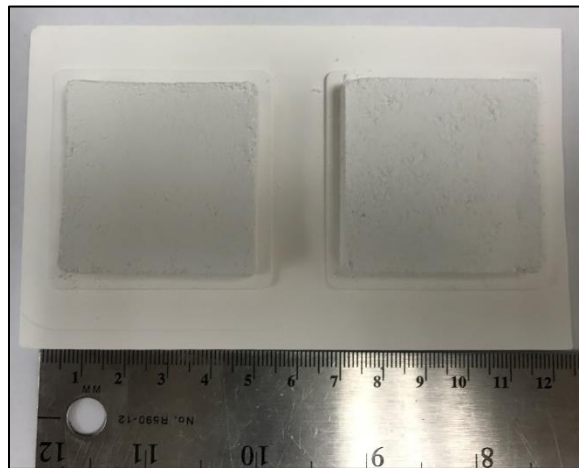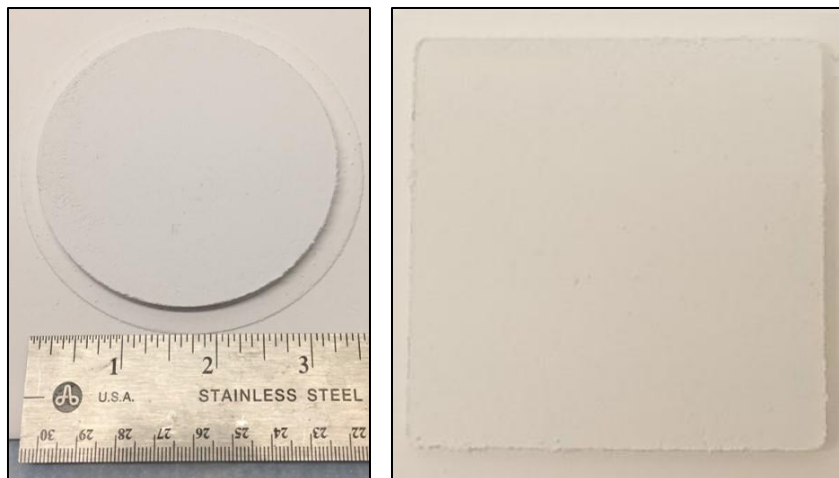

Figure 2.1.2-6. Two 41-mm square BaF$_2$ tiles created in the 2-inch mold shown in the previous figure.

Figure 2.1.2-7. An 87-mm diameter BaF₂ Disc and an 86-mm Square BaF₂ disc, both constructed using ceramic molds and a press. Both transmit very little visible radiation.

More than 80 sintering runs on barium fluoride were performed during this project to yield optimized tiles and to construct samples for testing. Detailed information on these tests may appear in a subsequent publication.

2.1.3   Barium Fluoride Sol-Gel Process

In an attempt to determine if processes other than molding and pressing could be used to fabricate rigid coatings, a sol-gel process was investigated. The sol-gel process has been known since the late 1800s and is a chemical solution process used to make ceramic and glass materials in the form of thin films, fibers, and powders. The sol-gel process uses either a chemical solution or colloidal particles to form an integrated network. In this project, we investigated the preparation of a barium fluoride sol-gel as a method of producing a rigid barium fluoride selective surface sample.

Figure 2.1.3-1. Barium fluoride sol-gel mixture used to determine if an alternative approach to sintering could be used to create a scattering layer.

The general procedure for preparation of a barium fluoride sol-gel is to add barium acetate, followed by trifluoroacetic acid, to isopropyl alcohol to form barium fluoride. The solution then reacts for several hours at room temperature to create a gel-like mixture (Figure 2.1.3-1). Part of this mixture was used to fill a 1-inch diameter aluminum mold to see if the gel would set in the mold to create a solid. However, this did not occur; after an overnight drying period, the gel collapsed into a liquid, resulting in most of the mixture escaping the mold. Another aliquot of the original mixture was used to successfully coat the surface of a glass disc using a spin coater (Chemat Technology, Model KW-4A) and allowed to dry at room temperature. Once dry, the material was placed into a furnace and sintered at 400 °C for 30

minutes. After sintering, the material was allowed to cool to room temperature, removed from the furnace, and analyzed.   The resulting sol-gel layer was visible, but very thin (100s of nanometers) and it was determined that repeated applications of the process to form a significant layer on the order of 100s of microns was not feasible, so this approach was dropped from further development.

2.2   Potassium Bromide (KBr)

Potassium bromide (KBr) has a very broadband transmission spectrum, which may be advantageous in reducing absorbed infrared radiation. For example, a tank coated with a KBr based cryogenic selective surface could maintain cryogenic temperatures closer to the earth than a BaF_2 coated tank. The Launch Service Program (LSP) showed interest in this possibility (see Section 4.2) and co-funded the development of a rigid KBr sample. KBr powder was purchased and, based on the barium fluoride work, was mixed with liquid. However, since KBr has high solubility in water, methanol was used as the liquid at approximately 12.8% (wt/wt). This mixture of KBr and methanol was placed into a round stainless steel or ceramic mold and either hand or mechanically pressed to compact the sample. A thin film of methanol was observed on top of the mixture and the sample was allowed to air dry overnight in an approved chemical fume hood. Once air dried, the sample was sintered using an optimized sintering profile (Table 5). The resulting sintered samples (see Figure 2.2-1) were not very structurally sound and they tended to easily break apart. KBr is a weak structural material, so the weakness of the sintered samples is a combination of inadequate particle connection and material properties.

Table 5. Optimized Sintering Conditions for Potassium Bromide Powder Sintering.

Temperature Profile	Comment
Ramp from RT – 65 °C	Hold at 65 °C for 30 minutes
Ramp from 65 °C – 125 °C	Hold at 125 °C for 10 minutes
Ramp from 125 °C – 225 °C	Hold at 225 °C for 10 minutes
Ramp from 225 °C – 325 °C	Hold at 325 °C for 10 minutes
Ramp from 325 °C – 425 °C	Hold at 425 °C for 60 minutes
Power off Furnace	Allow to cool overnight

Figure 2.2-1. A rigid, round, potassium bromide sintered tile in the form of a thin white disk.

2.3   Hafnium Oxide (HfO$_2$)

When we began to consider constructing cryogenic selective surfaces from oxides, we first reviewed the literature to find materials with wide enough spectral transmittance to stay cold in the presence of the Sun. Most oxides absorb either too much ultraviolet (e.g. TiO$_2$) or too much infrared (e.g. Al$_2$O$_3$ as sapphire). Hafnium oxide (HfO$_2$) appeared to meet the spectral requirements (its optical properties are not listed in the standard databases and we relied on vendor databases and subsequently made our own measurements, see Section 2.7) and a powder form of this material was obtained. We first attempted to make a sintered disk without adding liquid, but the result was not satisfactory (very weak mechanically), so we tried again with 10% (wt/wt) deionized water. The mixture of water and HfO$_2$ was stirred and ground and then placed into a ceramic mold and mechanically compacted. The pressed mixture was sintered using the sintering profile shown in Table 2.3-1. The melting point of hafnium oxide is 2758 °C, about 1400 °C above the melting point for barium fluoride's 1368 °C, so the maximum sintering temperature used (1050 °C) was probably inadequate, but was near the maximum achievable with our oven. Consequently, the resulting sintered tile (see Figure 2.3-1) was not very structurally sound but we were able to handle it for analysis without damage. The analysis of hafnium oxide indicated issues that maybe due to contamination (see Section 2.7) and we moved to yttrium oxide.

Table 2.3-1. Sintering Conditions for Hafnium Oxide Powder.

Temperature Profile	Comment
Ramp from RT – 250 °C	Hold at 250 °C for 45 minutes
Ramp from 250 °C – 500 °C	Hold at 500 °C for 45 minutes
Ramp from 500 °C – 750 °C	Hold at 750 °C for 45 minutes
Ramp from 750 °C – 1050 °C	Hold at 1050 °C for 45 minutes
Power off Furnace	Allow to cool overnight

Figure 2.3-1. A rigid, round, hafnium oxide sintered tile appearing as a white disk.

2.4   Yttrium Oxide (Y_2O_3)

Yttrium oxide (Y_2O_3), based on vendor data, has a broadband optical transmission band. It should not absorb significant solar radiation. We did find one paper on the use of yttrium oxide (referred to as yttria) [12] in IR windows and domes, that shows the material being brownish, but since our material was bright white we can only assume this prior work had contamination. Y_2O_3 is available in purer form than hafnium oxide and, while it has a slightly lower index of refraction (HfO_2 is about 2.1 in the visible while Y_2O_3 is about 1.9 and barium fluoride is about 1.47), it is lighter (density of HfO_2 is 9.7 gm/cc and density of Y_2O_3 is 5 gm/cc). We obtained Y_2O_3 powder and added approximately 10% (wt/wt) deionized water to form a mixture. The mixture was stirred, placed into a ceramic mold, and mechanically pressed. It was sintered using the temperature profile shown in Table 2.4-1. The sintered samples were not very structurally sound (an example is shown in Figure 2.4-1) but were stable enough to be analyzed; they tended to break apart without much force. As with hafnium oxide, we may not have been able to make the oven hot enough to achieve the degree of sintering required (the melting point of Y_2O_3 is 2425 °C).

Analysis (see Section 2.7) showed that yttrium oxide may meet the requirements for a cryogenic selective surface and further development occurred. More than 20 samples were constructed to better optimize the fabrication process and to construct samples for testing. We located a company that sells pressed Y_2O_3 disks and we ordered ten. They were roughly 40 mm in diameter and 3 mm thick and many were milky in appearance, indicating that they were fabricated with very high pressure and likely high heat. Most of the samples allowed significant transmission of light, but some did not. All of them were much stronger than any samples we fabricated in our oven. What this indicates is that there is likely an optimized sintering temperature profile that is higher than we can reach in our oven that will increase the strength of these tiles, but still maintain good optical properties. We have shown that by compressing Y_2O_3 powder at higher pressures that we can form stronger tiles with good optical properties, a promising result. However, we have had difficulties removing the pressed tiles from the molds and work is underway to resolve this problem.

Table 2.4-1. Sintering Conditions for Yttrium Oxide Powder.

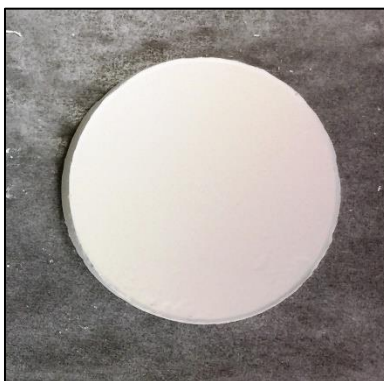| Temperature Profile	Comment
Ramp from RT – 250 °C	Hold at 250 °C for 45 minutes
Ramp from 250 °C – 500 °C	Hold at 500 °C for 45 minutes
Ramp from 500 °C – 750 °C	Hold at 750 °C for 45 minutes
Ramp from 750 °C – 1050 °C	Hold at 1050 °C for 90 minutes
Power off Furnace	Allow to cool overnight

Figure 2.4-1. A sintered yttrium oxide sample appearing as a bright white disk.

2.5   Barium Fluoride-Hafnium Oxide Composite

A series of experiments were conducted in an attempt to produce a composite selective surface material consisting of barium fluoride and hafnium oxide. The goal was to replicate the structure of white paint: scattering particles held in a transparent binder, where the hafnium oxide particles become the scattering particles and the barium fluoride is the transparent binder. This is achieved by mixing the two powders and then heating them such that the barium fluoride melts and then solidifies and holds the high melting point hafnium oxide particles in place.

Seventeen different parameter space variations were tried to create a best BaF_2-HfO_2 sintered tile. Three used water 10% (wt/wt), while the rest were dry. Various relative amounts of barium fluoride to hafnium oxide were tested ranging from eight parts barium fluoride to one part hafnium oxide (by weight) to equal parts of each. A variety of forces and sizes were tried, but most used the sintering temperature profile shown in table 2.5-1. The resultant tiles were not as strong as expected, possibly because the oven didn't get hot enough to actually melt the barium fluoride, but analysis showed a more serious problem. Energy dispersive x-ray spectroscopy (EDS) analysis of the resultant samples showed a loss of fluorine in the samples and indicated that barium hafnate had formed. Further confirmation of the presence of barium hafnate was attained by collecting X-ray powder diffraction data using a Malvern Panalytical Empyrean XRD. Such a result would change the optical absorption spectrum of the tile (see Section 2.7 for more discussion on this), likely for the worse, so we decided to discontinue this approach. An image of a typical barium fluoride – hafnium oxide sample is shown in Figure 2.5-1. We did fabricate one BaF_2-Y_2O_3 composite tile, but it displayed cracking and was not developed further.

Table 2.5-1. Sintering Conditions for Barium Fluoride – Hafnium Oxide.

Temperature Profile	Comment
Ramp from RT – 250 °C	Hold at 250 °C for 120 minutes
Ramp from 250 °C – 500 °C	Hold at 500 °C for 30 minutes
Ramp from 500 °C – 750 °C	Hold at 750 °C for 30 minutes
Ramp from 750 °C – 1000 °C	Hold at 1000 °C for 240 minutes
Power off Furnace	Allow to cool overnight

Figure 2.5-1. A sintered barium fluoride – hafnium oxide composite sample appearing as a white disk.

2.6   Potassium Bromide—Yttrium Oxide Composite

After noting the possible chemical reaction between BaF2 and HfO_2 during the sintering process, we decided to try KBr and Y_2O_3 instead, utilizing the much lower melting point of KBr (734 °C versus 1368 °C for barium fluoride). We hoped that by mixing these and then heating to melt the KBr that a structure could be created where the yttrium oxide particles were held in place by the KBr, yielding a relatively strong material with good optical properties. Eight variations of mixing ratios and pressures were used to construct sintered disks, with most using the sintering profile shown in Table 2.6-1. The resultant disks (one is shown in Figure 2.6-1) were strong enough to be handled and EDS results indicated that no detectable chemical reaction between the KBr and Y_2O_3 occurred. However, significant visible light transmitted through this sample, which we believe is due to poor mixing of the dry powders resulting in yttrium oxide deficient regions. We then added water to the mixture to try and improve the mixing and then noted that due to the high solubility of KBr that sintering was no longer required. This breakthrough is mentioned in Section 2.7 and described in more detail in Section 4.3.

Table 2.6-1. Sintering Conditions for Potassium Bromide – Yttrium Oxide.

Temperature Profile	Comment
Ramp from RT – 250 °C	Hold at 250 °C for 45 minutes
Ramp from 250 °C – 500 °C	Hold at 500 °C for 45 minutes
Ramp from 500 °C – 735 °C	Hold at 735 °C for 45 minutes
Power off Furnace	Allow to cool overnight

Figure 2.6-1. A sintered potassium bromide – yttrium oxide sample appearing as a white disk.

2.6   KBr – Y_2O_3 Spray-on Approach

While working with the KBr – Y_2O_3 mixtures we realized that sintering was not required to create a rigid tile. Potassium bromide can be dissolved in water and then the yttrium oxide particles added to form a white slurry. This "paint" can be applied to a surface and as it dries, the KBr will come out of solution and recrystallize, locking the Y_2O_3 particles in place. We tried applying this material to surfaces with a brush and soon moved to a sprayer to yield coatings. The coatings yield a better dispersion of Y_2O_3 in KBr than with the particle mixing approach.

We have not developed thick tiles using this approach, because we received co-funding from NASA's nuclear thermal propulsion program and they were interested in using it to coat multi-layer insulation to decrease heat flow into liquid hydrogen tanks. That work is described in Section 4.3. This area has several interesting applications including the construction of thick tiles by drying without heat, spray-on coatings to build up a cryogenic selective surface on a curved surface, and the use of dissolved KBr as a glue to adhere Y_2O_3 tiles to a metallic surface.

2.7 Analysis

This section presents our reflectance spectroscopy, Fourier transform infrared spectroscopy, and scanning electron microscope imagery results, but not our transmission measurements. We decided to omit the transmission measurements because, even though transmission is a key attribute of the scattering material, the measurements we obtained were not meaningful. When light impinges on a scattering material, it scatters in all directions, and for a thick sample (several millimeters) the light emerging from the back of the sample cannot be completely captured for measurement. In addition, for many of our samples, the transmitted light was so weak that measurement was difficult to quantify (compared to the incoming light) and the transmission was wavelength dependent, further complicating the measurement. In practice, we gave up on quantitative transmission measurement and used transmission as a relative measurement to compare samples, often just relying on a small bright light source (such as a flashlight) and visual appearance.
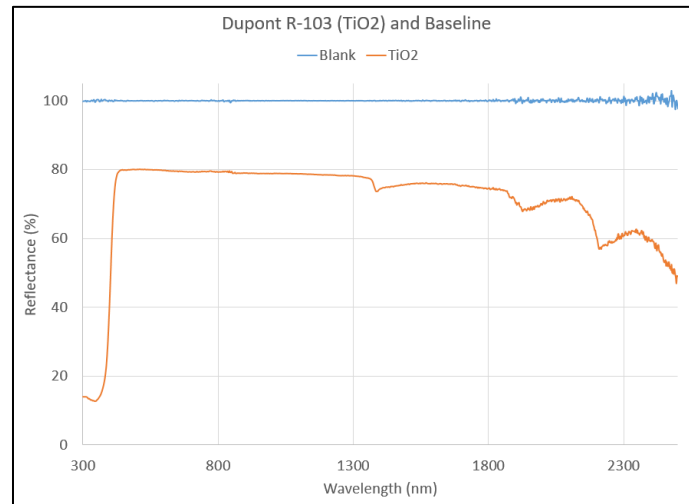
2.7.1   Reflectance Spectroscopy

Our analytic models require the complex index of refraction of a material over a wide range of wavelengths. For many optical spectroscopy materials, such as barium fluoride and potassium bromide, this information is available. However, for HfO_2 and Y_2O_3 this information is not, to our knowledge, in the published literature. If these materials were available as optical windows we could have made direct transmission measurements, however, they were only available as powders. Consequently, we had to resort to reflectance spectroscopy as a means to infer ultraviolet absorption. This is a somewhat ambiguous approach because reflectance from particles changes broadly with wavelength (Mie or Rayleigh scattering); however, it can provide a clear indication of the wavelength region where the material transitions from transparent to absorbing in the ultraviolet. That wavelength is important since it determines how much of the Sun's ultraviolet spectrum will be absorbed by the material.

Reflectance testing was conducted using a Jasco V-670 UV/Vis/NIR Spectrophotometer equipped with the ISN-723 Integrating Sphere attachment. The integrating sphere is 60 mm in diameter and coated with barium sulfate, operating over a 200 nm – 2500 nm spectral range. The spectrophotometer accepts samples ranging from 20 x 20 x 0.5 mm to 65 x 50 x 25 mm in size and includes an external detector instrument interface. A white reflective tile (Spectralon or NIST Traceable Standard) was used as a baseline material.

Figure 2.7.1-1 shows the measured reflectance spectrum for titanium dioxide (TiO_2) powder and for Spectralon. Since the device was calibrated with Spectralon the corresponding reflectance spectrum is 100%, indicating the device has been calibrated properly. The TiO_2 spectrum shows an abrupt change from low reflectance to high reflectance slightly above 400 nm, which is about where this material changes from absorbing to transmitting. This substantiates the use of a reflectance spectrometer to locate this ultraviolet transition. TiO_2 has minimal, if any, absorption from 500 nm to 2500 nm. The reflectance dips in the near infrared are interpreted as artifacts of the spectrometer since they are often seen and even occur sometimes when comparing Spectralon to Spectralon. Consequently, most of the reflectance spectra shown are limited to the 200 nm to 1200 nm range, allowing better inspection of the ultraviolet portion of the spectrum. In addition, the spectrometer is sensitive to the location of the scattering material since an integration sphere is collecting the reflected radiation. Powder samples have to be sandwiched between windows, which moves them

away from the integration sphere opening, lowering their measured reflectivity. This is why TiO_2, which is the basis for white paint, is only showing an 80% peak reflectivity in Figure 2.7.1-1.

Figure 2.7.1-1. The reflectance spectrum for titanium dioxide powder from 300 nm to 2400 nm showing the ultraviolet transition from absorbing to transmitting slightly above 400 nm and some machine artifacts in the infrared region.

The optical properties of barium fluoride and potassium bromide are well known, so the reflectance spectra for these powders are not shown in this report. However, we had to rely on the reflectance spectra of HfO_2, Y_2O_3 and ZrO_2 to determine if they could be considered for use as solar reflectors, because the available vendor and published data was ambiguous. Figure 2.7.1-2 shows the reflectance spectra for each of these three oxides as powders compared to Spectralon from 200 nm to 1200 nm. All three show better than 80 % reflectivity from 400 nm to 1200 nm, indicating minimal absorption in this region, as expected. What was surprising was the double dip shape in the ultraviolet reflectivity of HfO_2 and ZrO_2. Both show a reflectance dip between 350 nm and 400 nm and then the expected ultraviolet transition from transmissive to absorptive at about 250 nm for ZrO_2 and 230 nm for HfO_2. Yttrium oxide has only a single transition, rising to a maximum reflectivity at about 230 nm and then changing to absorptive for short wavelengths. We suspect that the double absorption dip for HfO_2 and ZrO_2 may be due to the presence of other oxides (contaminants) since the vendor supplied data sheets indicated that these might be present.

Also shown in Figure 2.7.1-2 is a plot taken from our Phase 1 NIAC, showing the percentage of total solar irradiance below a given wavelength in the ultraviolet. In our Phase 1 we desired minimal ultraviolet absorption and chose materials such as barium fluoride that have ultraviolet transitions below 200 nm (0.2 microns) where there is essentially no solar irradiant power in order to demonstrate the capability of our cryogenic selective surfaces. However, there is some available design space; in order to reach a cryogenic temperature of 90K the total absorption of solar radiation cannot exceed 0.4% to 0.9% (depending on the geometry). There will always be some infrared absorption and other sources of heat, but the 230 nm transition for Y_2O_3 only gives up about 0.15%, which leaves room for other heat sources. However, the double dip seen by the other two oxides raises serious concerns about their viability, especially for ZrO_2, which is a key reason we did not develop this oxide into tiles. Possibly a purer form of HfO_2 would yield a reflectance curve similar to that of Y_2O_3, but until a source is found for that, this reflectivity result biases further development towards yttrium oxide.
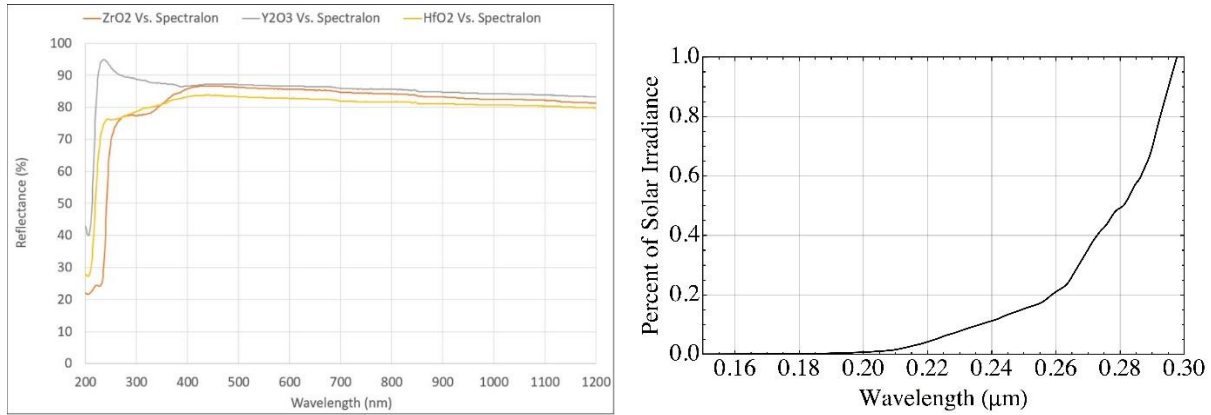
Figure 2.7.1-2. The reflectance spectra for zirconium oxide, hafnium oxide, and yttrium oxide from 200 nm to 1200 nm. All three show good reflectance from 400 nm to 1200 nm, but zirconium oxide and hafnium oxide have an unexpected absorption in the 300 nm region. Also shown is a plot of the solar irradiance percentage in the ultraviolet, indicating that a cryogenic selective surface should reflect radiation above about 250 nm. The reflectance spectra indicates that only yttrium oxide meets this criteria.

Figure 2.7.1-3 shows reflectance plots for our rigid barium fluoride materials. The left hand image shows plots for several samples, from 300 nm to 1300 nm displaying reflectivity values above that of Spectralon. The right plot was taken using a curved sample, so it was not close enough to the integration sphere to show the high reflectivity seen in the other plots. However, this plot extends down to 200 nm and continues to increase in reflectivity with decreasing wavelength, showing that the barium fluoride transition from transparent to opaque is below this wavelength (the transition occurs at about 140 nm). It should be pointed out that some of the apparent increase in reflectivity in the UV is due to a decrease in the reflectivity of Spectralon that starts around 300 nm.
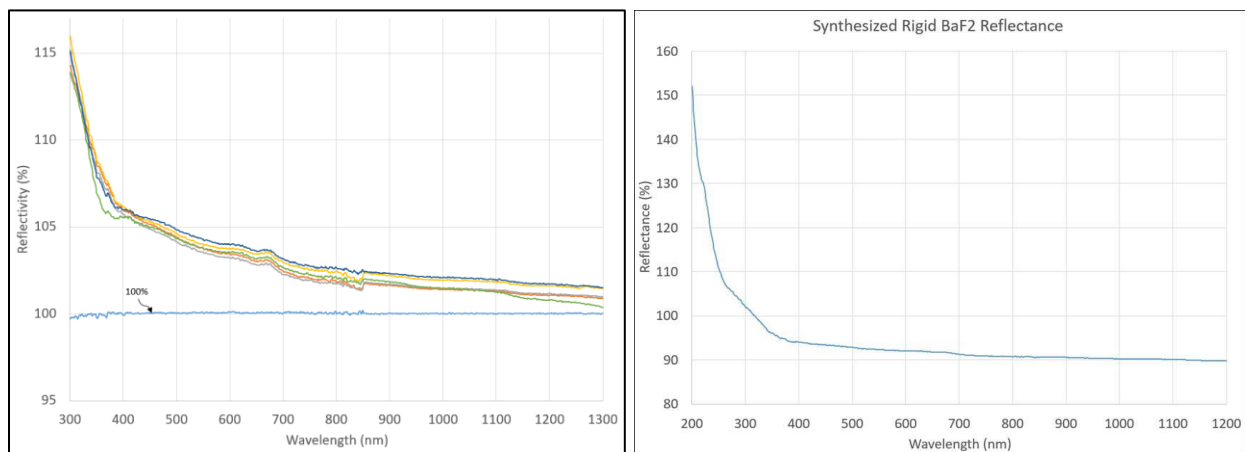
Figure 2.7.1-3. Reflectance spectra of several rigid BaF$_2$ samples showing high reflectivity, especially in the ultraviolet region.

Figure 2.7.1-4 shows reflectance spectra for a rigid hafnium oxide sample (left) and for rigid yttrium oxide samples (right). These plots are similar to the powder plots (though the hafnium oxide plot only goes down to 300 nm, missing the UV transition). The yttrium oxide plots are very promising, showing reflectance higher than Spectralon over most of the spectral range. Note that the ultraviolet transition can be smoothed (i.e. made less abrupt) by material stress. The rigid material ultraviolet transition appears to be more abrupt than for the powder, possibly indicating that the sintering process has decreased internal stresses within the particles.
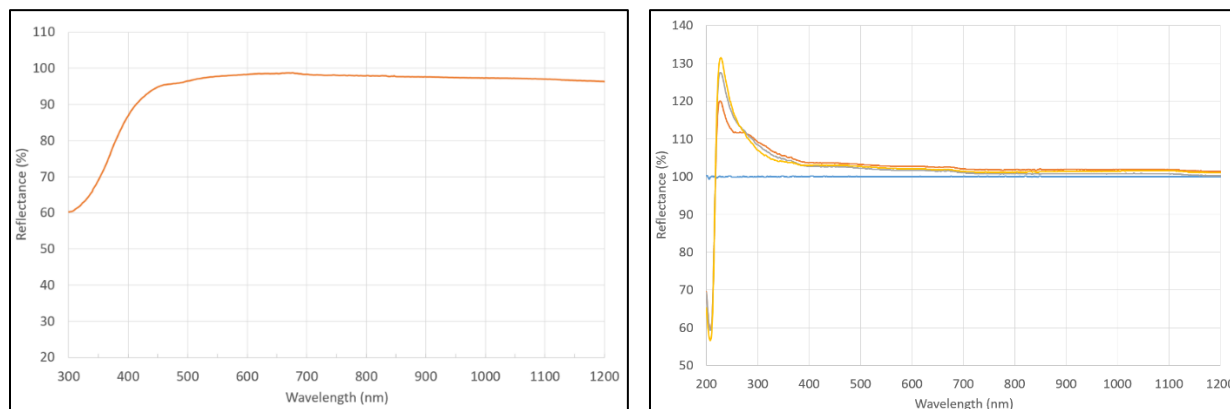
Figure 2.7.1-4. Reflectance spectra of Rigid HfO$_2$ (left) and rigid Y$_2$O$_3$ (right).

Figure 2.7.1-5 shows reflectance spectra for several rigid barium fluoride – hafnium oxide composite samples (left) and a barium fluoride-yttrium oxide composite sample (right). The plots for BaF$_2$ –HfO$_2$ drop faster in the ultraviolet and result in poorer reflectance at 300 nm than for the pure HfO$_2$ case, but this difference does not infer much until the BaF$_2$ – Y$_2$O$_3$ plot is considered. Neither BaF$_2$ nor Y$_2$O$_3$ should produce a drop in reflectance between 300 nm and 400 nm. This is disturbing until we recall that the EDS data shows a loss of fluorine in the BaF$_2$ –HfO$_2$ case indicating the creation of a barium-hafnate compound. This compound, and its twin for the yttrium case, are likely causing this additional absorption of radiation in the 300 nm range.
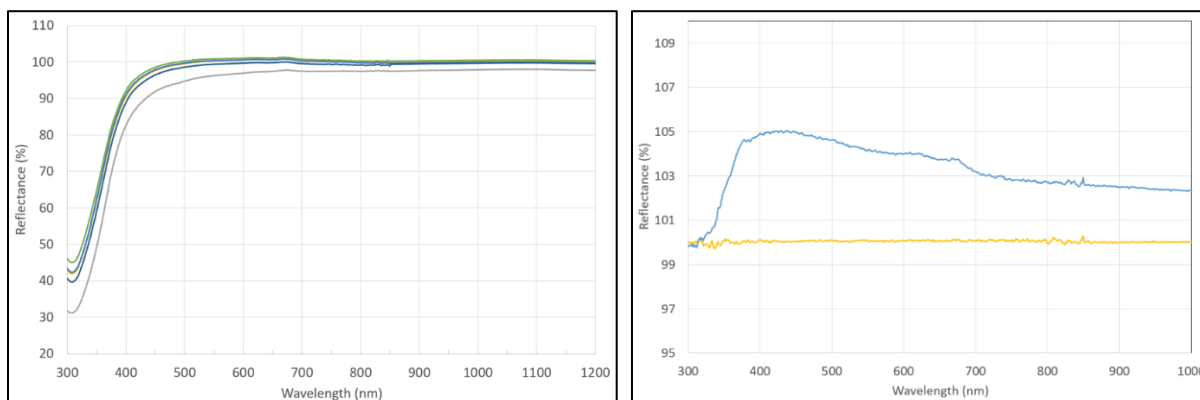

Figure 2.7.1-5. Reflectance spectra of several rigid BaF$_2$ –HfO$_2$ composite samples (left) and a rigid BaF$_2$ – Y$_2$O$_3$ composite sample (right).

Figure 2.7.1-6 shows the measured reflectance spectrum for a rigid potassium bromide – yttrium oxide composite. Comparing this reflectance plot to the one shown in Figure 2.7.1.4 for rigid yttrium oxide shows that the presence of the potassium bromide has had minimal effect on the reflectivity; possibly causing a slight drop in reflectivity but not changing the location of the ultraviolet transition. This indicates, and is supported by the EDS data, that no reaction is occurring between the potassium bromide and the yttrium oxide in the creation of this sintered tile. Figure 4.3.2-2, in the application section, shows a potassium bromide-yttrium oxide reflectivity plot using our spray-on approach. That plot also shows no change in the location of the ultraviolet transition, though the overall reflectivity is lower due to the thinness of this coating (less than 100 microns for the spray-on coating versus a few millimeters for the tile).
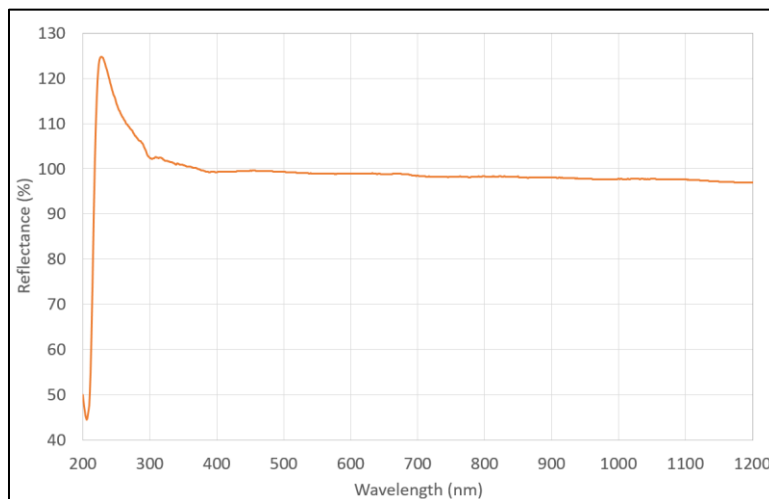
Figure 2.7.1-6. The reflectance spectrum of a rigid KBr – Y_2O_3 composite sample.

2.7.2   FTIR-ATR Spectroscopy

Reflection spectroscopy only provides optical information out to 2.5 microns. In order for a material to be useful as a cryogenic selective surface it must not absorb significant infrared solar radiation well beyond 2.5 microns. Ideally, the transition from transparent to absorbing should not start until after 9 microns in wavelength (less than 0.1% of the Sun's irradiance is at wavelengths longer than 9 microns). Since we did not have optical data on the oxides we measured their infrared absorption spectra using a Fourier Transform Infrared Spectrometer (FTIR) with an Attenuated Total Reflectance (ATR) cell. Specifically we used a Bruker ALPHA Fourier-Transform Infrared Spectrometer equipped with a Platinum-ATR attachment. Data was collected from 2.5 µm – 25 µm.

Figure 2.7.2-1 shows the measured infrared absorption data for barium fluoride powder along with a calculated infrared absorption spectrum for a 200-micron thick optical window using available optical data for barium fluoride. Ideally, these two spectra should have similar shapes, but the FTIR spectrum has absorption anomalies at 2.5 microns and 6.5 microns. Ignoring these the measured absorption does increase with longer wavelengths, but the lack of a match between these implies that the FTIR-ATR data should not be taken as definitive. The ATR uses the evanescent field from a diamond light guide to measure infrared transmittance and the large index mismatch between barium fluoride and diamond may explain the poor signal to noise in the barium fluoride measurement. The other plots shown below for the oxides are significantly better and this may be a result of the higher index of the oxides, allowing better index matching to the diamond.
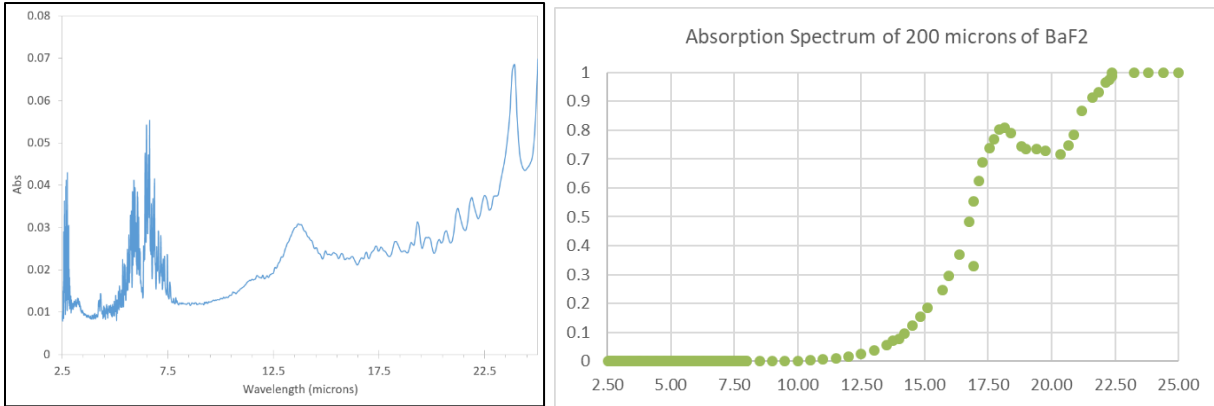
Figure 2.7.2-1. The measured infrared absorption spectrum for BaF$_2$ powder compared to the absorption spectra for a BaF2 window. The measured spectra has some artifacts and doesn't match the known spectra well, but the overall increase in absorption starting around 12 microns is apparent.

Figures 2.7.2-2, 2.7.2-3, and 2.7.2-4 show the FTIR-ATR measured absorption spectra for HfO$_2$, Y$_2$O$_3$ and ZrO$_2$, respectively. All three measured spectra appear to have lower noise than the barium fluoride spectra and show minimal absorption below 10 microns, indicating that these three materials have infrared transmission properties appropriate for use as cryogenic selective surfaces. Hafnium oxide starts to absorb at about 12 microns and shows a couple of absorption peaks in the long wave region of the spectrum, which is typical of long wave band pass materials. Yttrium oxide appears to have a softer transition, but that might be an instrument artifact. One might argue that the long wave transition begins at 15 microns, which would be a positive attributed for this material. Note that we assume the small peak at 6.4 microns is a machine artifact based on the barium fluoride data. Zirconium oxide shows a spectrum similar to hafnium oxide, with a transition starting around 12 microns.
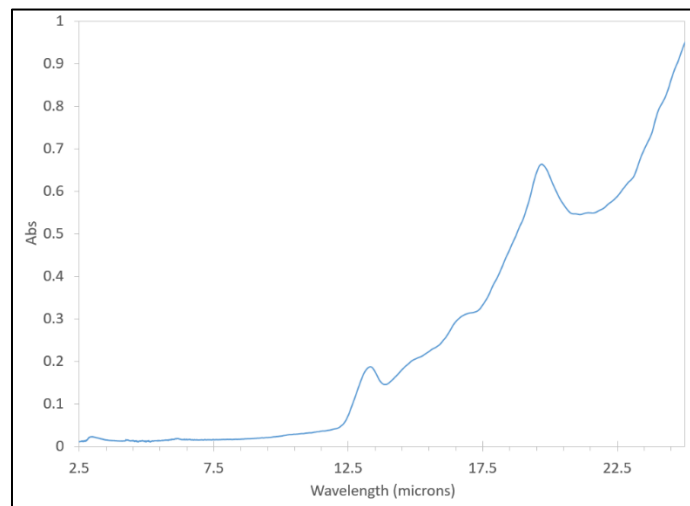

Figure 2.7.2-2. The measured absorption spectrum for HfO$_2$ powder showing an initiation of absorption at about 12 microns.
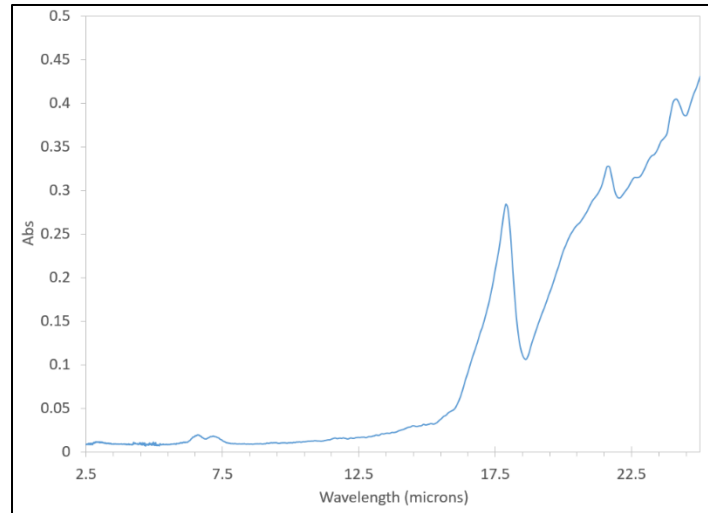
Figure 2.7.2-3. The measured absorption spectrum for Y_2O_3 powder showing an initiation of absorption beyond 12 microns.
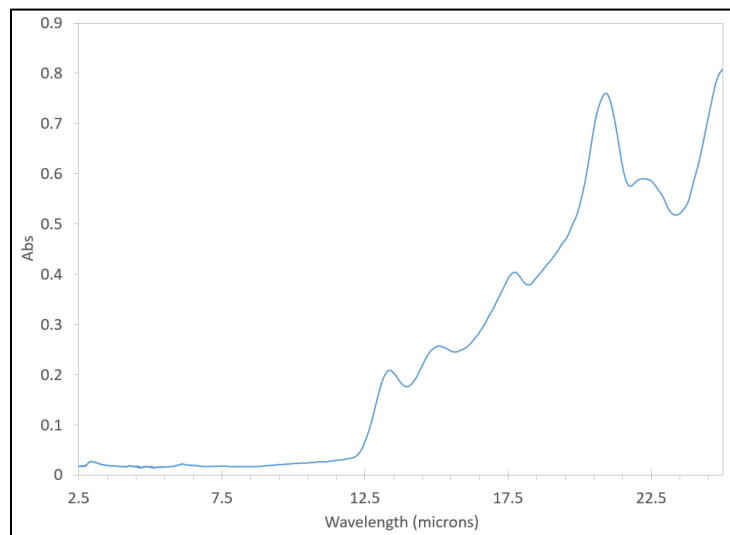

Figure 2.7.2-4. The measured absorption spectrum for ZrO_3 powder showing an initiation of absorption at about 12 microns.

### 2.7.3   Scanning Electron Microscope Imagery

The reflectivity of powders and sintered materials is affected by the size of the scatterers. Mie scattering theory indicates that the peak scattering wavelength for a sphere corresponds to the circumference of that sphere and that the scattering will drop as one-over the wavelength to the fourth power for longer wavelengths (Rayleigh scattering). The peak of the Sun's irradiance spectrum is about 480 nm, indicating that our scatterers should be about 150 nm in diameter. This was rarely the case and reflectivity measurements showed biases to longer or shorter wavelengths and the corresponding images usually indicated the presence of larger or smaller structures than were ideal. So imagery is important to understanding the reflectivity of the materials, as well as observing cracks and non-uniformities.

Images of powders and produced samples were collected using a scanning electron microscope (JEOL Model JSC-7500F Field Emission Scanning Electron Microscope (SEM)) equipped with an Energy Dispersive X-Ray Spectroscopy (EDS) detector. X-Ray Powder Diffraction (XRD) data was collected using a Malvern Panalytical Empyrean XRD. The XRD data is not provided explicitly in this report, but was used to draw conclusions that have been discussed in the pertinent sections.

Figure 2.7.3-1 shows four SEM images of barium fluoride particles. The upper left image shows purchased powder (Sigma Aldrich). These particles are 200 nm to 400 nm in size, which is larger than desired. We measured the reflectivity of these powders [11], and of rigid tiles fabricated from them, and showed that the peak scattering was in the near infrared. This is expected from particles of this size, but it is not desirable for the current application. We began fabricating our own barium fluoride powder because of supply issues with Sigma Aldrich and soon found that we could control the size of the barium fluoride crystals by changing the conditions of the synthesis process. Figure 2.7.3-1 shows SEM images of synthesized particles when the temperature of the solutions was lowered (upper right), when the reagents were diluted (lower left) and when the solutions were warmed (lower right). None of these yielded perfect sizes, however, a greater number of small particles were now present and the corresponding reflectivity spectra showed peaks shifted into the ultraviolet (see Figure 2.7.1-3).
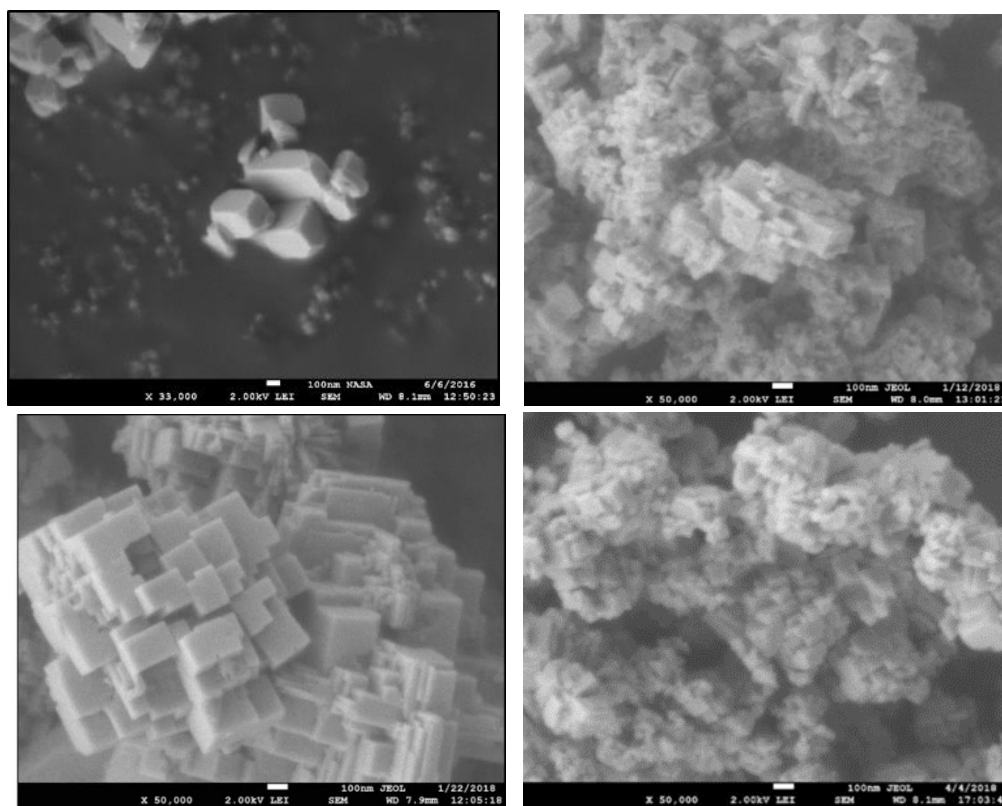

Figure 2.7.3-1. SEM Images of four barium fluoride powders. The upper left was purchased and shows particles larger than 200 nm. The other three were synthesized under varying conditions; upper right used cold solutions, lower left used dilute solutions, and lower right used warm solutions. Each of the synthesized particles has different shape and size characteristics.
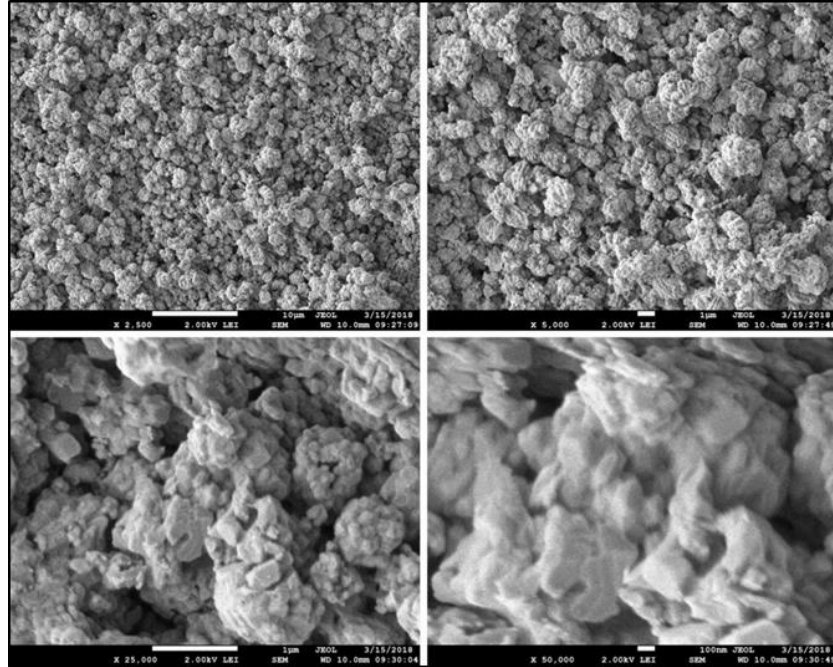
Figure 2.7.3-2. SEM images of sintered barium fluoride fabricated from synthesized powder. Images are at four magnifications showing a uniform distribution of 1-micron balls composed of smaller, 100 nm to 200 nm particles.

Figure 2.7.3-2 shows SEM images of a region on a sintered barium fluoride tile fabricated from synthesized particles. The imagery shows a uniform distribution of roughly 1micron balls composed of smaller, randomly shaped, 100 nm to 200 nm particles. The smaller particles show significant sintering and are melting together forming the 1 micron balls. The scattering from this rigid structure shows significant ultraviolet reflectivity, indicating the smaller entities are strongly contributing to the scattering.

Figure 2.7.3-3 shows SEM images of commercial potassium bromide where the average particle is large, over 100 microns. The left image is powder and the right image is from a tile fabricated from this powder. Testing showed relatively poor reflectivity from these particles and from the tiles, likely due to the large particle size. We demonstrated that this rigid tile could be used to reflect 10 micron radiation by using a soldering iron as an infrared heat source and an infrared camera to observe the scattering, but that is not pertinent to the current need for a solar reflector.
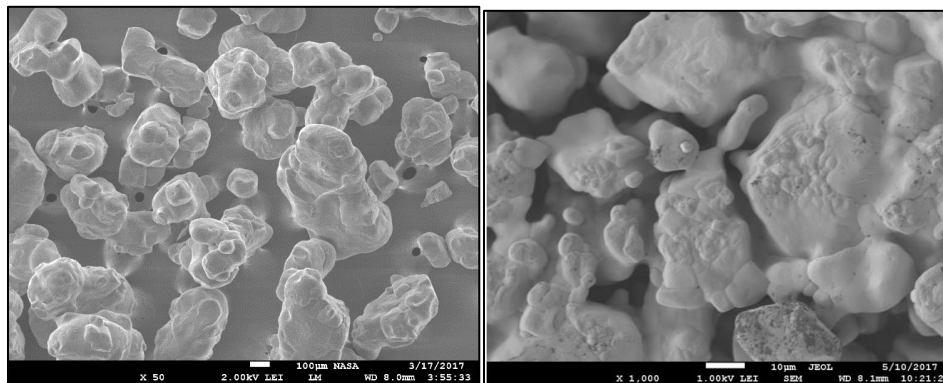
Figure 2.7.3-3. SEM images of commercial KBr powder and a sintered tile fabricated from this powder. The particles are large, averaging over 100 microns in size.

26

Purchased hafnium oxide and yttrium oxide particles were small, roughly 100 nm in diameter. Figure 2.7.3-4 shows SEM imagery for a sintered tile composed of hafnium oxide. The particles are uniformly distributed, however, there isn't much evidence of sintering, likely due to the limitation of our oven and the high melting point of hafnium oxide. Figure 2.7.3-5 shows SEM imagery for yttrium oxide where 100 nm structures are seen and there is clear evidence of sintering between the particles. Reflectivity measurements of yttrium oxide, coupled with these SEM images indicate that the yttrium oxide particles may be smaller than desired. Larger particles or longer sintering may be necessary.
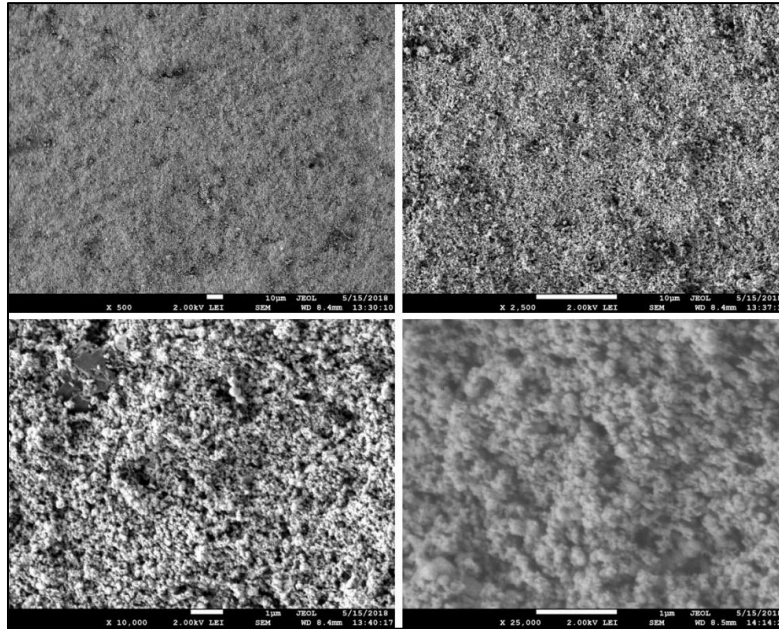

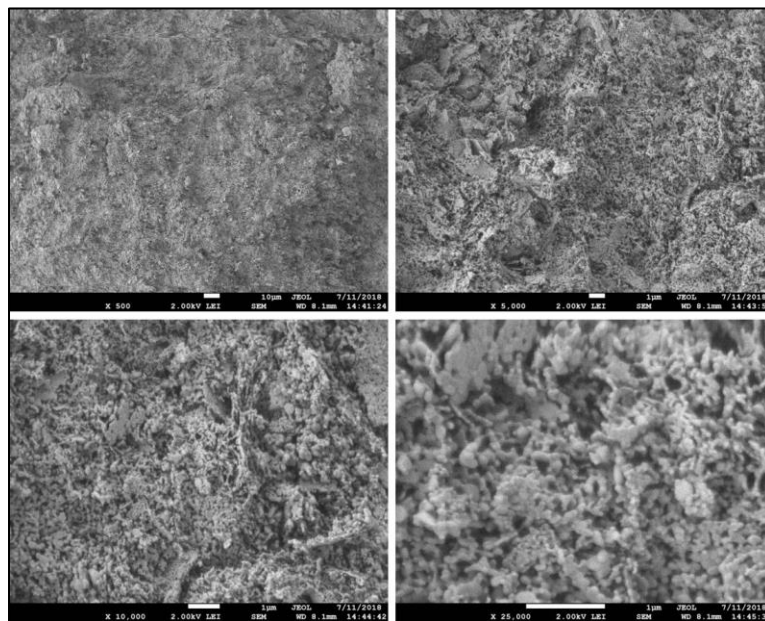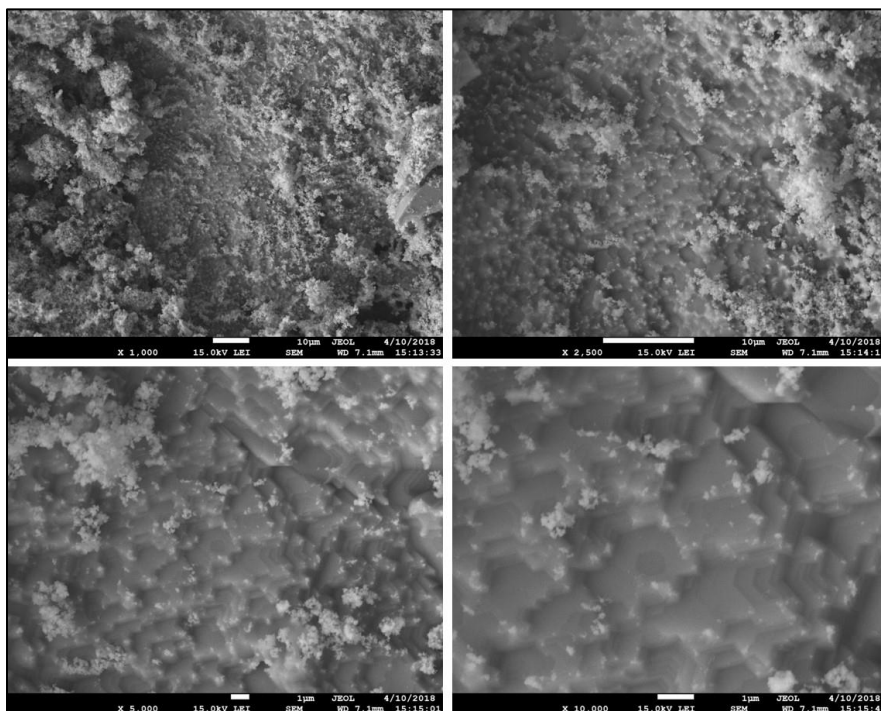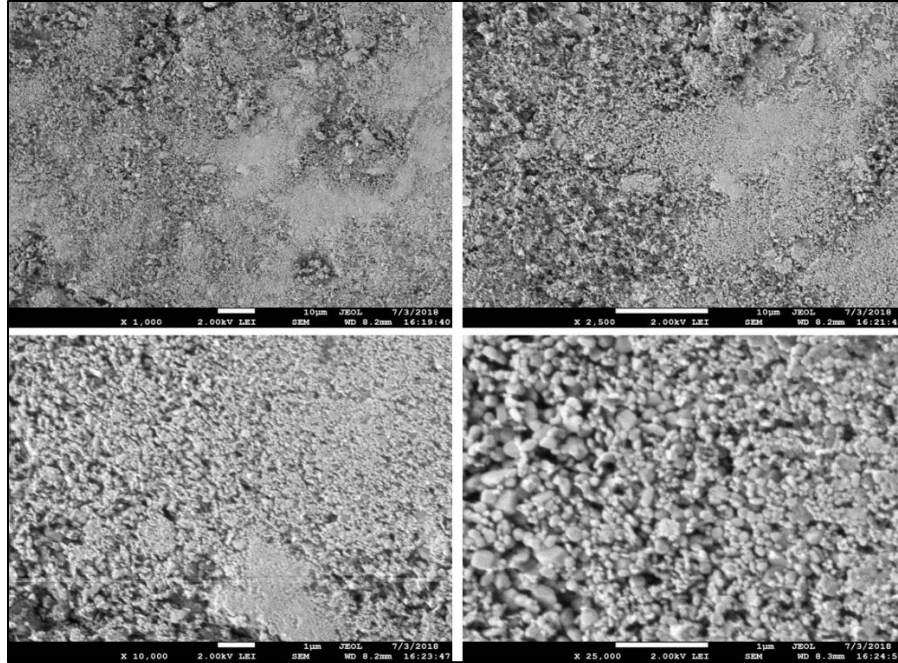*Figure 2.7.3-4. SEM images of a rigid HfO$_2$ sample showing particles about 100 nm in diameter.*

Figure 2.7.3-5. SEM images of a rigid Y$_2$O$_3$ sample showing 100 nm structures with clear evidence of sintering.

Figure 2.7.3-6 shows SEM images for a rigid BaF_2- HfO_2 composite sample. Recall that this mixture was heated to allow the barium fluoride to partially melt and hold the hafnium oxide in place. The SEM imagery shows that this did occur, the barium fluoride is seen to form sheets across the material, holding the hafnium oxide particle in place. However, there is clumping of the hafnium oxide, indicating that better dispersion is needed. This composite was not developed further, because EDS and XRD data indicated that the sintering process caused the formation of barium hafnate. This unwanted molecule may be responsible for the decrease in ultraviolet reflectivity seen in this composite sample. A similar effect was seen in the $BaF_2 - Y_2O_3$ composite and it was also dropped from further development.

Figure 2.7.3-6. SEM images of a rigid $BaF_2 - HfO_2$ composite sample showing that in some locations the barium fluoride did melt and holds the hafnium oxide particles in place, however, the overall surface is not uniform. The hafnium particles are clumped and not well dispersed.

Figure 2.7.3-7 shows SEM imagery of a rigid $KBr - Y_2O_3$ sample. The yttrium oxide appears to be distributed throughout the rigid sample but small areas of clumping were observed. The average particle size of the yttrium oxide appears to be 100 nm and the sample maintained the particle-like structure, which is desired. However, the amount of KBr does not appear to be sufficient to hold the yttrium oxide in place. A more promising $KBr - Y_2O_3$ SEM is seen in Figure 4.3.2-6, showing the result of our spray-on approach.

Figure 2.7.3-7. SEM images of a rigid KBr – Y$_2$O$_3$ composite sample.

2.8   Mechanical Testing

At one time during the project, we believed we had come close to optimizing rigid barium fluoride for use as a cryogenic selective surface. We were creating custom particles and had a good grasp of the pressure and sintering temperature profile needed to create material with a best combination of strength and optical properties. So, we decided to move to the next stage in development and have mechanical testing (ASTM C133) performed to determine the flexural strength of our new material. Testing was performed using an Instron 5982 load frame equipped with a 100kN load cell. Figure 2.8-1 shows the samples, an image of the Instron testing a sample, and the resultant broken samples. The graphs of the test results are shown in Figure 2.8-1 and the tabulated results, alone with test specimen information, are shown in Figure 2.8-3.   The flexural strength is not high, similar to that of chalk, but adequate for handling.
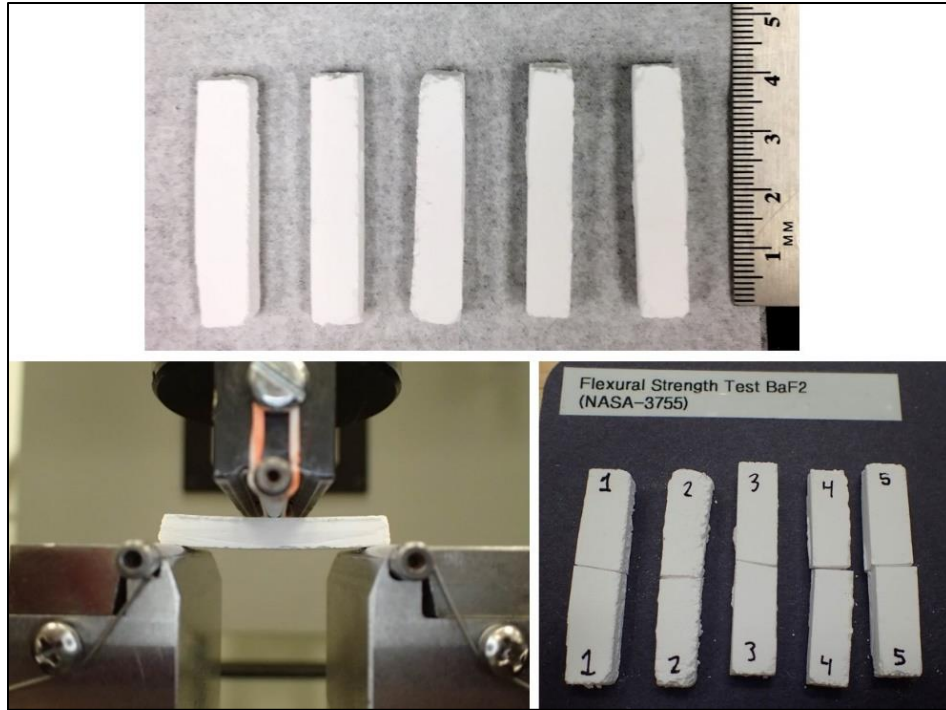
Figure 2.8-1. Five 4-cm long pieces of rigid barium fluoride were tested in an Instron, a machine that slowly deforms a material in a bridge configuration until the material breaks. The machine snapped the five samples roughly along their centerlines.
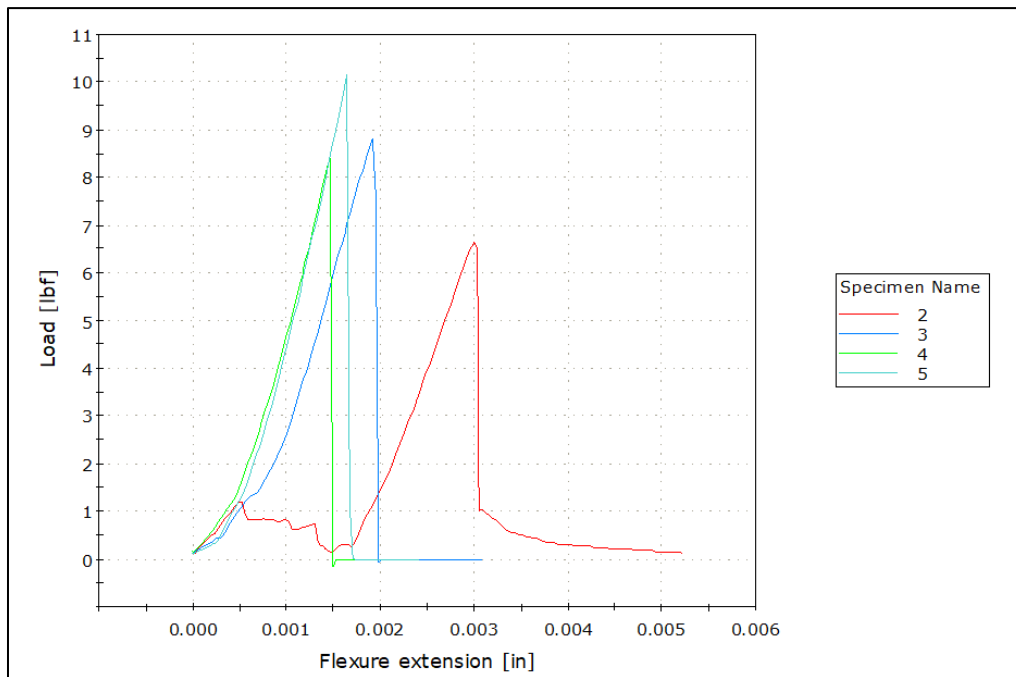

Figure 2.8-2. Four plots are shown of the applied force versus the flexure extension for each of the four samples. These plots show the deformation of the samples growing with increasing force, until they break.

Table 2.8-1. The dimensions of each sample are shown in this table along with the maximal load and flexural stress measurements.

	Specimen label	Thickness [in]	Width [in]	Support span [in]	Rate [in/min]	Maximum Load [lbf]	Flexural Stress [psi]
1	2	0.222	0.316	1.40	0.020	6.63	895
2	3	0.221	0.325	1.40	0.020	8.81	1166
3	4	0.222	0.294	1.40	0.020	8.39	1216
4	5	0.221	0.321	1.40	0.020	10.13	1357

2.9   Machining

Tiles formed from molds have fabrication limitations making it difficult to meet stringent size and shape parameters and to include holes. Consequently, we explored ways to machine the fabricated tiles, concentrating on barium fluoride. The tiles need to stay clean and dry, so a vacuum chuck was designed and fabricated, see Figure 2.9-1, to hold a specific tile. The machined tile was a square, high-compression force, barium fluoride, sample and it was milled with a 0.250-inch three-flute end mill running at high speed. Multiple passes were used and the results show minimal chipping of the tile (Figure 2.9-1).
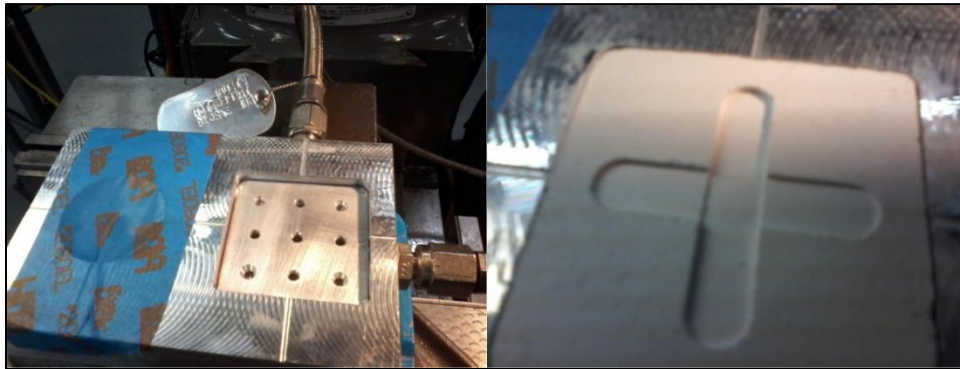

Figure 2.9-1. A vacuum chuck used to hold a barium fluoride tile for machining and the tile showing machined slots.

More complicated shapes were cut in the tiles in order to support testing. Figure 3.1-3 shows two barium fluoride tiles that have been machined to fit together, forming an internal void where a temperature sensor can be placed. These tiles were machined using another custom vacuum chuck, this one is shown in Figure 2.9-2. This particular barium fluoride sample was an early tile and was not as homogeneous as the one shown above. It was carefully machined using a four-flute end mill running dry at high speed. Further machining tests showed that the surfaces of the tiles can be contoured into curves allowing tiles to fit onto curved surfaces. Examples are shown in Figure 2.9-3. In addition, it was necessary for testing that the tiles be suspended in a deep space environment and this required small holes. These holes were drilled using a 0.053-inch carbide bit running at high speed to minimize chipping on the back side of the tile.
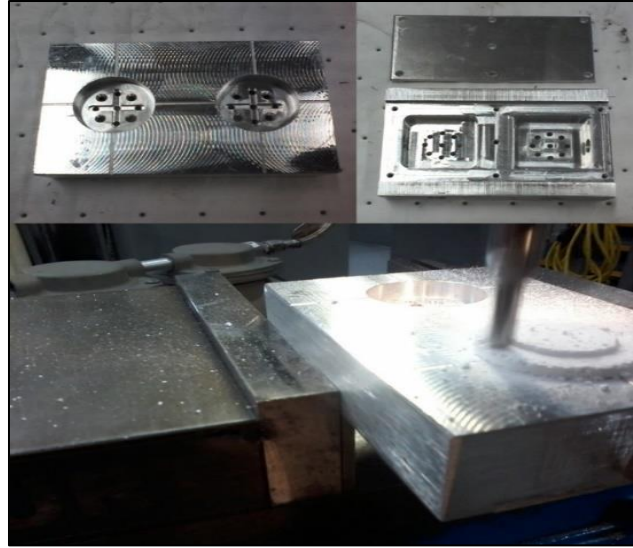
Figure 2.9-2. Machining Sintered, Round BaF$_2$ Sample.
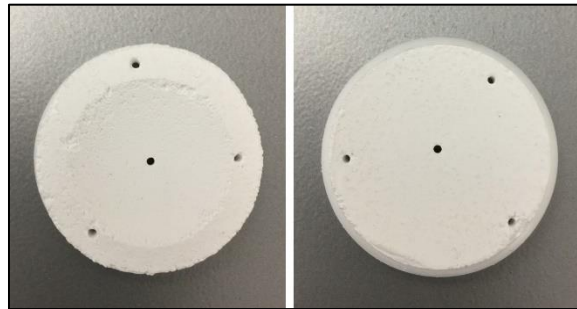
Figure 2.9-3. These images show tiles that have had curved surfaces machined into them and holes drilled through them.

The tiles were also hand cut for some tests.   A German style jewelers saw was used to cut the Instron test samples shown in Figure 2.8-1. Also, some tiles were fragile and in those case we used hand-held drill bits and other tools to careful modify the tiles so they could be tested.


2.10 Silver Deposition

An area that has been neglected in the prior discussion is the silver, or highly reflective, backing needed on our cryogenic selective surface in order to reflect long wave infrared radiation. As will be seen in the test section, this silver is important for operation of the cryogenic selective surface and is a part of our predicted performance modeling (see Figure 1-2.). We have modeled the performance [6] with other metals, but silver is the preferred option. Fortunately, our spray-on technique adheres reasonably to silver, allowing the scattering material to be directly applied to a silver-coated surface. However, this approach will not work for a tile sintered in an oven at high temperature.

One attempt at creating a silvered surface on barium fluoride tiles was to use a PVD Products Physical Vapor Deposition System (Serial Number J00S3318) and a silver sputter target. The samples were wrapped with aluminum foil so that only the surface to be coated was visible. Two different sputter coating methods were used in the coating process. One method utilized a single, 38:45 sputter time (sputter rate = 0.86 Å/second) and a second method utilized multiple sputter cycles, each 10 minutes in length (with the exception of the final cycle, which was 8:45 in length) with 10 minutes in between sputter cycles. All samples had a final silver film thickness of approximately 2000 nm (Figure 2.9-1).

Figure 2.9-1. Silver-coated BaF$_2$ samples showing a grey color.

Figure 2.9-2 shows an SEM image of the deposited silver on barium fluoride. The silver coating appears to be continuous, though contoured due to the underlying particle structure of the sintered barium fluoride tile. We did not measure the reflectivity of this coating because it appears to have oxidized upon removal from the deposition chamber. Future work will be needed to place a silver coating behind the particle scatterer. This might be done by deposition, or by forming the sintered tile directly on a silver surface, or possibly melting a sheet of silver onto the tile. Another option might be to use dissolved KBr as a glue to attach the tile to a silvered surface.
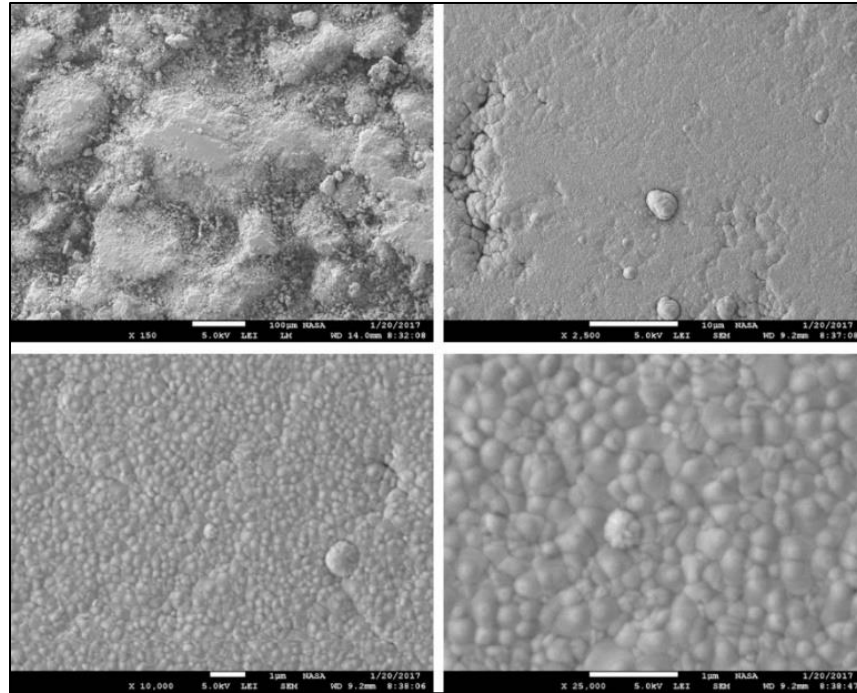
Figure 2.4.2.2-2. SEM images of the silver coating deposited onto the sintered barium fluoride material. The silver coating appears to be continuous, though contoured due to the underlying particle structure.

2.10   Water Removal

As mentioned in the simulated deep space testing section, for a few months we became very concerned about water retention in our cryogenic selective surface coatings. This led to an effort to determine if water was present, and if so, how to remove it. Most of that work was documented in our Phase 1 NIAC project "Solar Surfing" final report [10]. We subsequently realized that water retention may not be a serious issue and that even barium fluoride (and hopefully potassium bromide) will give up any adhered water molecules when exposed to long-term deep space vacuum. Yttrium oxide, like almost all substances, holds on to a small amount of water (we measured 0.21% by weight in a 16.5 hour vacuum exposure test), but due its hydrophobic nature we have minimal concerns about it not drying when exposed to vacuum. Hopefully, continued vacuum chamber, cryogenic testing, will yield low temperature results indicating the absence of water.

3   Simulated Deep Space Testing.

An ideal test of our new cryogenic selective surfaces would be to expose a coated object to deep space solar irradiance, far from any infrared emitter, and measure the equilibrium temperature of that object. Assuming the long wave emittance is known, and recalling that the energy emitted at equilibrium equals the energy absorbed, the object temperature is directly related to the absorbed power. However, such a test was beyond the funding available for this project, so instead we created a simulated deep space environment. We used a cryocooler to chill a small aluminum container in a vacuum chamber to temperatures in the 20-30K range. We suspended our coated sample within this chamber and allowed it to cool down over a period of 2-3 days. Then a light source was turned on, irradiating the coated object and causing it to warm. Its equilibrium temperature was measured and from that, the absorbed power estimated.

3.1   The First Year of Testing

During the first year of the Phase II project, our testing was limited to using light sources within the chamber, because pressure vessel concerns prevented us from installing a window on the cryogenic chamber. This chamber was under vacuum and modifying a vacuum chamber requires substantial time and resources. We tried a variety of light sources, which were low enough in power that the cryocooler could handle the heat load, and eventually settled on a 375 nm LED from Thor Labs. More than a dozen rounds of testing, each requiring system modifications and 2-4 days of chill down, were conducted during the first year of the project. The discussion below only pertains to the final most successful tests.
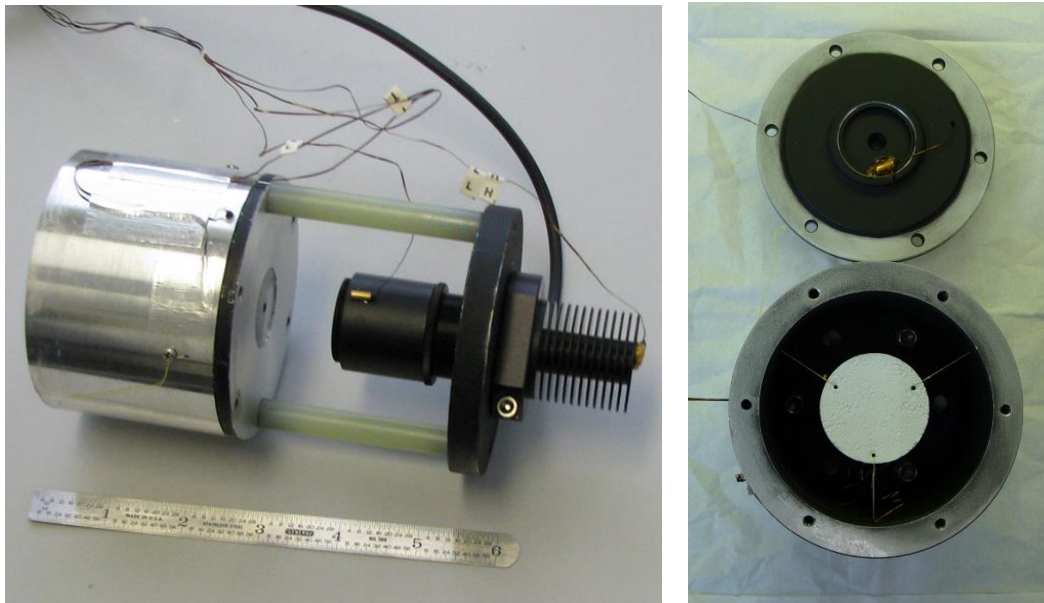
Figure 3.1-1. There are two photos shown. One shows an ultraviolet LED with an optics module attached to a sample holder such that the ultraviolet emission is directed into the sample holder through a small aperture. The other photo is the sample holder with the lid taken off, showing the sample suspended by thin strings within the sample holder.
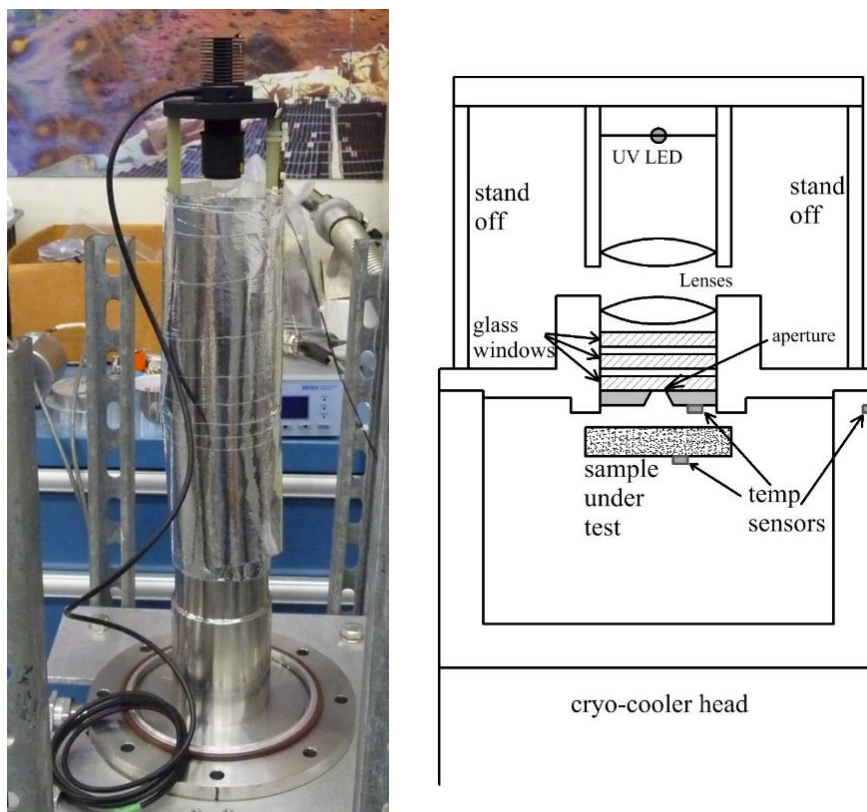
Figure 3.1-2. This image is of the ultraviolet LED on top of the assembled test system. A sketch shows the various components within the test system including the ultraviolet LED, lenses to collimate and focus the light, an aperture, glass windows as thermal barriers, the sample under test, and three temperature sensors.

Figure 3.1-1 shows this ultraviolet LED, with an attached optics module, positioned over the sample enclosure. This is an early version with the optics attached to the LED. Also shown in Figure 3.1-1 is the aluminum container that was attached to the cryocooler with the lid lifted off. The inside has been painted black and the sample hung with very fine string. The lid shows that a temperature sensor has been located on a window covering the aperture through which the ultraviolet light will enter the container and hit the sample. Figure 3.1-2 shows the LED and optics module on top of the system assembly, with the vacuum shroud removed. Also shown is a sketch of the internal components; temperature sensors, optics, and the aperture (this is a later design where a lens has been moved to the sample enclosure to help minimize infrared emission by chilling the lens). This test is described in our publication [11], so details will not be repeated here, but in summary, about 17 mAmps of 375 nm radiation were launched onto a BaF_2 sample and it only rose in temperature from about 44 K to 49 K, indicating, after analysis, that less than ¼% of the irradiated energy was being absorbed. This successful test was the first experimental verification of our new cryogenic selective surface, but was limited to low power and a narrow spectral source.

In the final version of this test, the sample, composed of BaF_2, consisted of two pieces that were machined to form a cavity, see Figure 3.1-3. One piece had a lip removed and a channel cut into it for the temperature sensor and the second BaF_2 piece had a matching depression cut into it. Both pieces had small outer holes drilled into them, allowing them to be tied together with the temperature sensor inside, ready for mounting into the sample enclosure. The temperature sensor used was a Scientific Instruments Si-410 AA cryogenic temperature sensor. It has four 36 gage phosphor bronze leads and a case size of 0.1-inch diameter and 0.25 inches long. It has excellent performance. Our test data shows resolution in the 20-100 K range of 0.01 K and when dipped in LN_2 yielded the correct value to within experimental error.
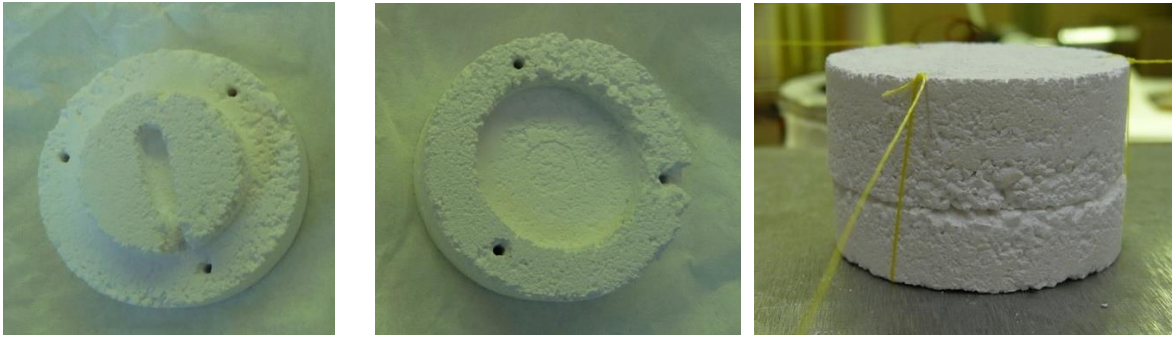
Figure 3.1-3. The two piece BaF$_2$ sample, showing the cutouts and the assembled version. The cut-outs are made to yield a small enclosed volume within the assembly where the temperature sensor is located. The two pieces are tied together with fine string.

3.2 Second Year of Testing

3.2.1 The Test System

During the second year of the project, we were able to obtain a vacuum shroud with a window allowing the use of an external light source; a Xenon lamp with a spectrum similar to that of the Sun. This testing is more indicative of the actual deep space performance of the coatings, to within the limitations of the test set-up, and is discussed below in some detail. The goal is to highlight the performance of our new materials, while trying to clearly describe the shortcomings of the experiments. An even higher fidelity system, with enhancements incorporated based on this testing, is in construction at the Glenn Research Center and will be utilized during follow on coating development and testing.

Figure 3.2.1-1 shows a CAD model of the new vacuum shroud with the cryocooler cold finger (copper colored). Designing the vacuum shroud to have two pieces eased assembly of the test system. It allowed the sample chamber, with its temperature sensor wiring to be installed on top of the cold-finger, with the lower shroud section in place. The wires could then be routed (using feedthroughs) out of the chamber through the ports in the lower vacuum shroud section. Then, after the components were in place the upper shroud section could be lowered onto the assembly without affecting the system wiring. The upper section has a port on top allowing the attachment of an optical window.
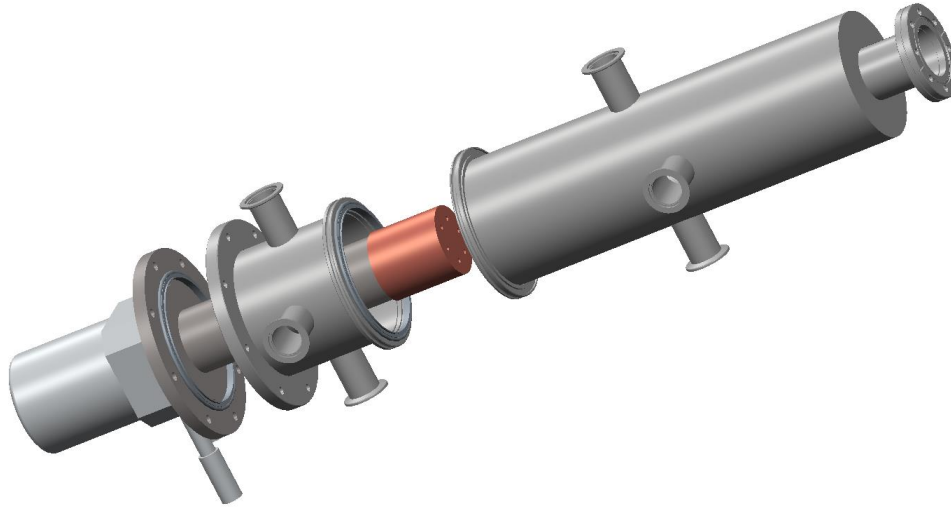
Figure 3.2.1-1. This CAD model shows the cold finger (copper) with a two-piece vacuum shroud.

A 250-Watt Xenon lamp was purchased, shown in Figure 3.2.1-2, to provide the illumination. This lamp arrived with an ultraviolet filter and an intensity adjustment mechanism, both of which were removed. Without the UV filter the lamp has a spectrum similar to that of the Sun as measured with a UV-visible Ocean Optics Spectrometer. Note that this is a potentially dangerous light source and should only be used by personnel with training in the use of very bright light sources and the associated hazards. A higher fidelity solar simulator was purchased by the Glenn Research Center for their test system. It should be pointed out that solar simulators are rated for use over the 300-1400 nm region and were originally developed for the development of photo-voltaic detectors. This does not mean that a solar simulator is a poor simulation of the Sun beyond 1400 nm, since both are effectively blackbodies. However, consideration of the intervening optical materials and their transmission is necessary to allow long wavelength radiation to reach the sample being tested.

Figure 3.2.1-2. A Xenon Lamp was used as a solar simulator and a sapphire viewport was used to seal the vacuum chamber, but allow the radiation from the Xenon lamp to enter.

A sapphire, vacuum rated, viewport was purchased from MDC Vacuum Products to place on top of the vacuum shroud. This viewport is uncoated sapphire with a transmission range from the ultraviolet out through the mid-infrared. It has a 2-inch open aperture and has a 4.47 inch DS stainless steel flange, as shown in Figure 3.2.1-2.

Figure 3.2.1-3 shows three images. The left image is the complete test structure with the vacuum shroud, the sapphire window, and the light source. A support structure was built to carry the weight of the light source and ensure that it is in a fixed position. There was concern that the light emerging from the Xenon lamp could become misaligned, changing the amount of light hitting the sample under test, so effort was expended on the design of the Xenon lamp mounting system. The middle image shows the internal test structure with the vacuum shroud and sapphire window removed and the right image shows a system cutaway. The copper colored section, which is wrapped in the center image and not visible, is the cold finger of the cryocooler. Sitting on top of this is the sample chamber (to be discussed more below) and on top of that is the optics tube. The optics tube consists of a thick-walled tube of aluminum with a thin walled-tube of optical components held inside of it. The thick-walled tube allows heat to be drawn towards the cryocooler to help chill the optics. In some of our prior testing the primary source of heat warming the sample was infrared radiation from warm optical components and we hoped to minimize this in the present design by keeping the optical elements cold.
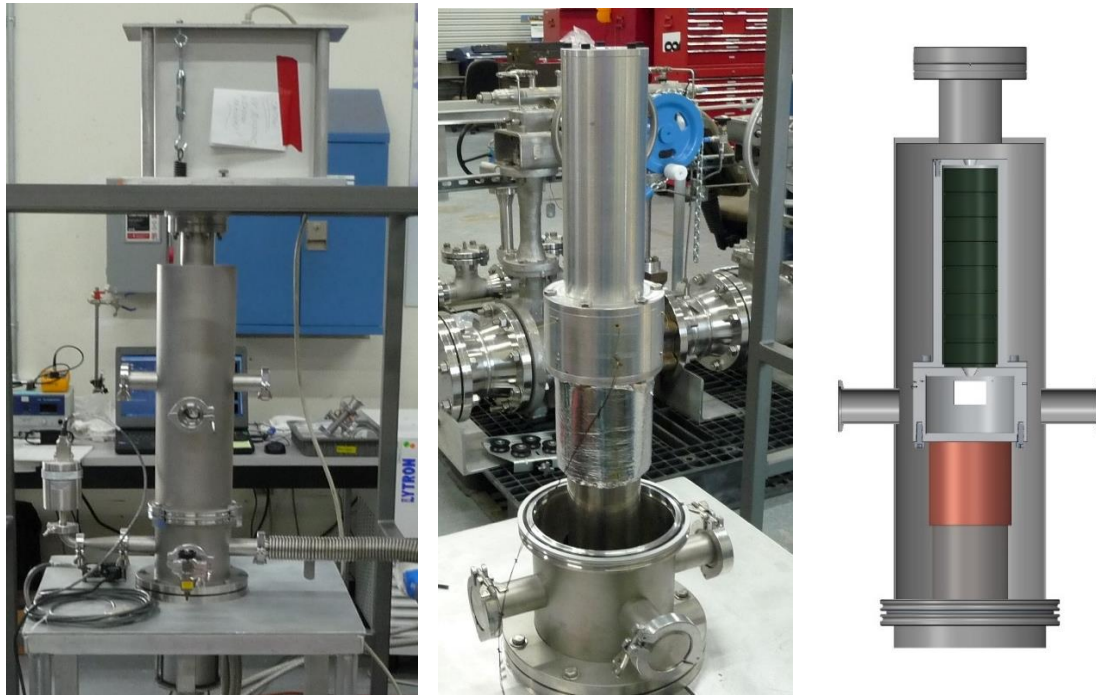

Figure 3.2.1-3. The vacuum shroud with the sapphire window and light source support on top. In the center is the test assembly without the shroud, showing the sample chamber and the optics outer tube. The right sketch shows a cut-away displaying the sample location, optics tube, and cryocooler.

Figure 3.2.1-4 shows the system optical components. This optical system had two goals: 1) to relay the light from the Xenon lamp to the sample under test and 2) to minimize background infrared radiation from reaching the sample. The light emerging from the Xenon Lamp is diverging and a lens was used to focus it onto an aperture at the top of the lens tube. The purpose of the aperture is to block background infrared from entering the optical tube. The light then passes through two CaF_2 windows that serve as long wave infrared blocks. They absorb long wave radiation, become

warm and then re-radiate this in all directions, so each window reduces the amount of long-wave radiation that propagates down the optical tube. A pair of UV grade fused silica lenses are used to relay the Xenon lamp output to the next aperture, where the light passes through two more CaF_2 windows before reaching the sample. All of the internal optical components are held in 2-inch diameter Thor Labs anodized aluminum lens tubes.
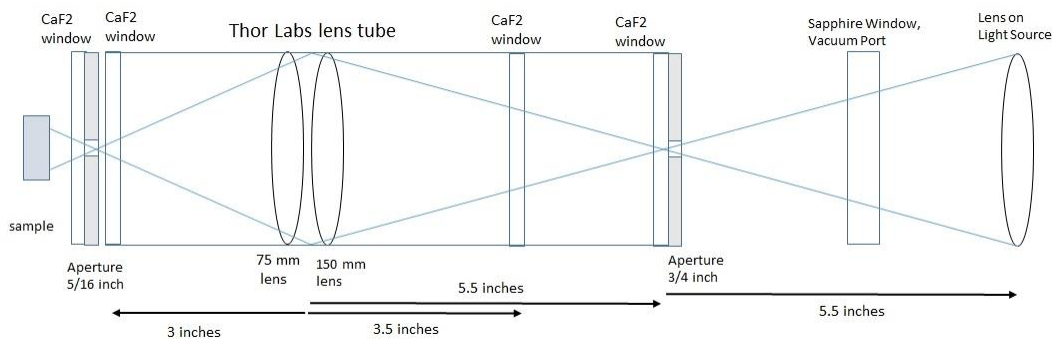

Figure 3.2.1-4. This sketch is of the components making up the lens assembly. Starting from the right, a lens is used to focus the output from the lamp through the sapphire window and onto an aperture. The light then expands and is refocused by two more lenses, onto a second aperture behind which is the sample. Four CaF_2 windows are used as thermal barriers.

A serious shortcoming of the system design is that measuring the amount of radiation reaching the sample from the Xenon light source is difficult. In order to make this measurement, the vacuum shroud and optical components are removed, so that the sample chamber can be replaced with supportive rods/struts. Then the optics components are put back in place and the Xenon lamp turned on. This allows a detector to be placed at the sample location and used to measure the total optical power. However, the system then needs to be disassembled again, so the sample chamber and sample can be put back in place, and then reassembled. The concern is that during disassembly and reassembly that the lamp or optical system are not in the same location as during the measurement. The system optics and apertures were selected to allow for some translational motion of the light source, so we do not believe that the measurement is in error. However, it would have been preferable to be able to make this measurement without such disruption to the test system. The next generation system in construction at the Glenn Research Center will not have this issue.

The optical power measurement was made with a Newport calibrated silicon (UV enhanced) photodetector (our specific photodetector is no longer stocked, but Newport sells a similar item, part number 818-UV/DB) and two broadband ND2 neutral density filters (Edmund Optics part number 88-281). Using this combination the detector measured 87 microamps. In order to convert this to Watts, we first used the measured Ocean Optics spectrum of the light source and summed the detector response against this light spectrum for each wavelength band. This yielded a figure of 0.3 Amps/Watt for the portion of light we could measure (about 190 nm to 1100 nm). We then modelled the light source as a 5800 K blackbody, used that spectrum instead of the measured one, and obtained the same responsivity, 0.3 Amps/Watt. We then noted that the UV grade fused silica windows were the infrared limiters in the optical system and that they transmit out to about 4 microns. So we added the additional irradiance in the 1100-4000 nm band to the wattage calculation and obtained a detector conversion factor of 0.24 Amps/Watt. Assuming the Edmund Optics ND filters are ND2 over the detector's detection bandwidth (this is what was advertised by the manufacturer, but detailed ND values were not provided with the components), then each ND drops the optical power by a factor of 100. So the total optical power hitting the sample is 0.000087*100*100/0.24=3.6 Watts.

3.2.2   The First Barium Fluoride Test

In April 2018 we conducted our first test of the system using a barium fluoride rigid sample. Figure 3.2.2-1 shows the sample in the enclosure, held in place with three fine strings. The top of the sample enclosure, i.e. the lid, shows the last CaF_2 window and a temperature sensor attached to the window. There is also a temperature sensor attached to the lid itself and one attached to the sample, as seen in the right-hand image in Figure 3.2.2-1. Small coils of wire were used to increase the conductive path length of the wire to help minimize thermal connection between the temperature sensor and the enclosure. A fourth temperature sensor was attached to the enclosure itself. It is on the outside and does not appear in these images.
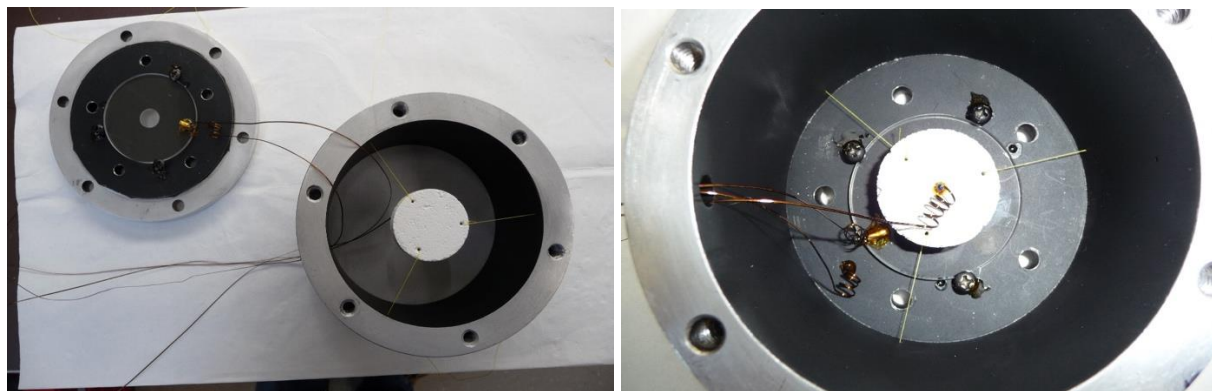
Figure 3.2.2-1. A BaF$_2$ sample is mounted in the sample enclosure using fine strings and top and bottom views are shown. These views indicate the locations of the temperature sensors, one on the sample, one on the last CaF$_2$ window, and one on the aperture.

After assembling the system, it was pumped down, allowed to stabilize, and then the chiller was turned on. This sample required two days to chill-down, eventually reaching 24 K while the three other temperature sensors were between 20 and 22 K. When the light source was turned on there was a rapid rise in all of the temperatures, as seen in Figure 3.2.2-2, primarily caused by the additional heat load on the cryocooler. Surprisingly, the BaF$_2$ sample, which we expected to stay relatively cool heated far above our expectations, reaching a temperature of 173 K.
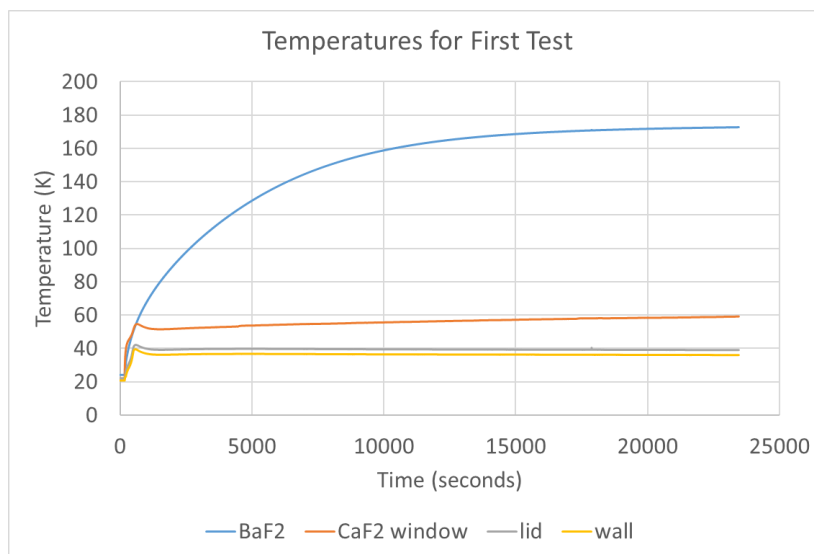
Figure 3.2.2-2. This plot shows the temperatures for the first test. When the Xenon light is turned on the sample enclosure wall and lid increase from 20K to 40 K, the CaF$_2$ window increases from 20K to about 60 K, and the sample takes about 6 hours to reach a temperature of 173K.

The emissivity of BaF$_2$ at low temperatures (long wavelength) is about 0.9. The sample is 32 mm in diameter and 12 mm in height and has a total surface area of 0.0028 m^2. So the total power emitted by this sample, assuming the measured temperature is equal to the surface temperature, is given by the Stefan-Boltzmann law as 0.13 Watts. At steady state, the emitted power must equal the absorbed power, indicating that 3.6% of the irradiated power impinging on this sample is being absorbed, which is better than the state-of-the-art, but not as low as expected.

In April we attributed the excess absorption of radiation by BaF$_2$ to water. A very thin water film (2-3 molecules) across the BaF$_2$ surface area could account for the absorbed power. We discussed the potential water issue in BaF$_2$ in the final report on our NIAC study entitled "Solar Surfing" [10]. Believing water was a potentially limiting problem in the use of barium fluoride, we sought other materials and began to consider oxides.

3.2.3   Yttrium Oxide Testing

After some searching we chose Y$_2$O$_3$ (yttrium oxide), a high index, hydrophobic, broadband material. We manufactured sintered rigid versions of this material from purchased powder, as shown in Figure 3.2.3- 1 (details on manufacturing are provide elsewhere in this report).
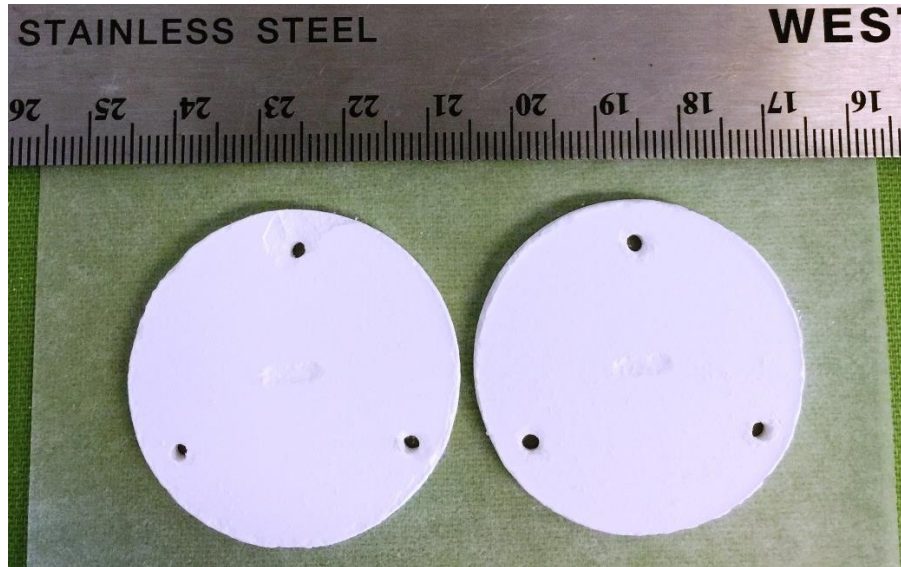
Figure 3.2.3-1. Yttrium Oxide rigid tile samples are shown. They are round disks, about 4 cm in diameter, and each has three small holes drilled through it near the outer edge, so that they can be tied together to enclose a temperature sensors and suspended using fine string.

We placed this material into the test system in early August 2018. After pump-down and two days of chilling, the lamp was turned on. To our surprise, the Y_2O_3 sample heated more quickly than the BaF_2 sample, rising to 130 K within 2000 seconds of turn-on. So, we turned the lamp off and re-evaluated the testing. We noticed that the temperature sensor inside of the sample was responding to the lamp very quickly, at nearly the same time as the other temperature sensors. This was unexpected because there should be some delay as the sample heats before the temperature sensor responds. So we guessed that infrared radiation might be making its way through the samples and heating the temperature sensor directly as well as the varnish used to hold it in place (the varnish can be seen in Figure 3.2.2-1).

In order to test this we wrapped the temperature sensor with silver foil and then installed it between two Y_2O_3 rigid samples, as shown in Figure 3.2.3-2. The idea here was that the Y_2O_3 would scatter the short-wave radiation and the silver would reflect any long-wave that made it through the Y_2O_3. This sample was installed, and after about a 2-day chill down, the lamp was turned on. Now, after 2000 seconds, as seen in Figure 3.2.3-3, the sample was below 80K. We turned the lamp off at about 9000 seconds and believe that the sample would have stabilized at about 120 K, a much more encouraging result.

This sample is 38 mm in diameter and 13.5 mm thick, yielding a surface area of 0.0039 m². Again assuming a long wave emissivity of 0.9 and that the outside of the sample is at a temperature of 120 K, the emitted power is 0.041 Watts, or about 1.1% of the irradiated power. This was a significant improvement and indicated that the temperature sensor (or the varnish, or both) were absorbing infrared radiation. The Sun's total deep space irradiance at 1 AU is about 1366 W/m^2, so a 38 mm diameter object would intercept 1.55 Watts of power. In this case, the Y_2O_3 sample, assuming the test data is valid, would absorb 0.017 Watts of power and would come to an equilibrium temperature of about 96 K—almost cold enough for liquid oxygen (LOX).

Figure 3.2.3-2. A temperature sensor wrapped in silver and then installed between two Y_2O_3 rigid samples.
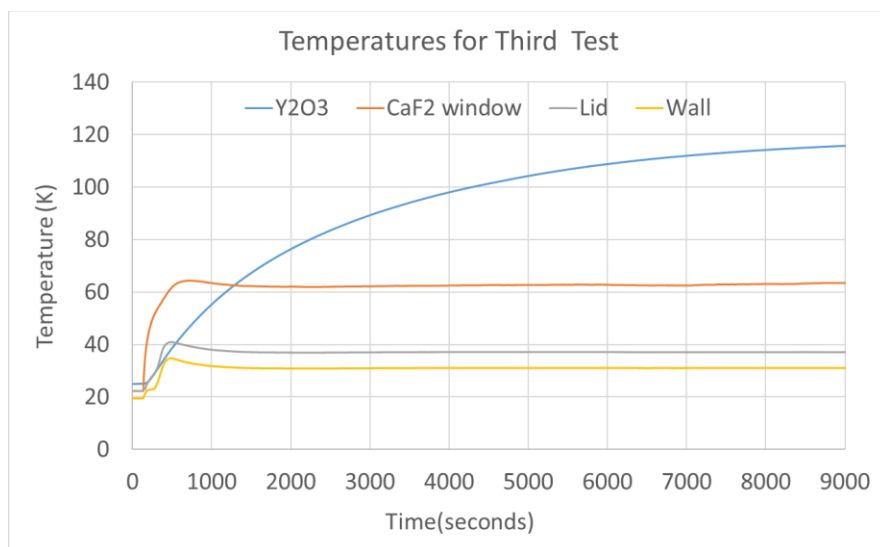

Figure 3.2.3-3. Temperatures for the second Y_2O_3 test. When the Xenon light is turned on the sample enclosure wall and lid increase from about 20K to between 30 K and 40 K, the CaF_2 window increases from 20K to about 60 K, and the sample takes about 2.5 hours to indicate that it would have stabilized at about 120 K.

3.2.4   Second BaF$_2$ Test

We then decided to retest barium fluoride with the temperature sensor wrapped in silver foil. Figure 3.2.4-1 shows the wrapped sensor located inside of a pair of BaF$_2$ rigid samples. The barium fluoride samples were from an early fabrication run. They were fragile and had some chipping, but they were available and we had access to the cryocooler so we ran the test with them. We evacuated the system on a Friday and didn't turn on the cryocooler until Monday, allowing this sample to be exposed to vacuum for the weekend, hopefully removing any excess water. Chill-down took 3 days, more than for the other tests, possibly due to the thick nature of this sample (the stacked sample is 32 mm in diameter and 23 mm thick).

Figure 3.2.4-1. Barium Fluoride sample with the temperature sensor wrapped in silver foil. One image shows the temperature sensor nestled in a cutout in the center of a rigid barium fluoride disk and the other images shows a second barium fluoride disk placed on the first one to form a test sample where the temperature sensor is in the center of the sample.
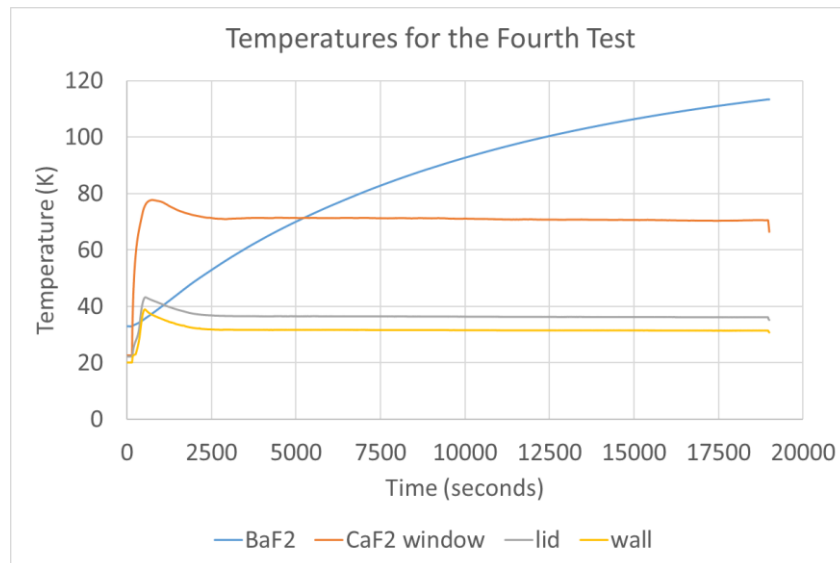

Figure 3.2.4-2. Temperatures for the fourth test; BaF2 with a silver wrapped temperature sensor. When the Xenon light is turned on the sample enclosure wall and lid increase from about 20K to between 30 K and 40 K, the CaF$_2$ window increases from 20K to about 70 K, and the sample takes about 5 hours to indicate that it would have stabilized at about 125 K.

Figure 3.2.4-2 shows the results, where we turned off the Xenon lamp just before 19000 seconds. The warm up of the sample fits an exponential curve with a limiting value of 125 K. So using that value and a surface area of 0.0039 m^2 there is an emitted power equal to 0.049 Watts. So this sample is absorbing 1.4 % of the irradiant power. If this sample were in deep space, at 1 AU, facing the Sun, it would have 1.1 Watt hitting it, would absorb 1.4% of that, and come to an equilibrium temperature of 94 K.

The results are impressive and better than the state of the art, but should be better. Based on the significant reductions in temperature obtained by wrapping the temperature sensors in silver foil, we noted that we should have wrapped the

wires connected to the sensor in silver as well. Looking at Figure 3.2.4-1, the temperature sensor lead is dark and likely absorbs long wave radiation, causing it to heat and to transmit this heat to the temperature sensor. So a next test will be carried out with the temperature sensor wires directed out of the back of the sample and wrapped in silver foil to help shield them from the radiation. Hopefully, this will lead to even lower temperature performance.

3.3 Development of a High Fidelity Low Temperature Solar Simulation Test Cell

As a part of the NIAC Phase 2, the Glenn Research Center (GRC) began the development of a high-fidelity low-temperature solar simulation test cell (see Figure 3.3-1). The objective was to provide a test location to demonstrate the performance of the cryogenic selective surface material by incorporating a low-temperature sink mimicking deep space while providing the equivalent of 1 sun (i.e. the solar heat flux at the distance between the earth and the sun) in the appropriate wavelengths at high vacuum.

Research into solar simulators quickly revealed that there were no certified solar simulators that were designed to operate in a vacuum. Thus a series of lenses and filters were designed to allow the solar simulator energy to get into the vacuum chamber, but keep out most other energy (see Figure 3.3-2). The lenses on the system are configured to maintain the light beam similar to as shown in Figure 3.2.1-4, with the exception that the solar energy will be recollimated at the end to help mitigate placement errors of the sample. A cryocooler provides the low temperature sink and is thermally anchored to the test chamber. Recent tests with the cryocooler have produced temperatures lower than 20 K. The system will be painted black internally and lessons learned from the KSC testing are being incorporated throughout the system.
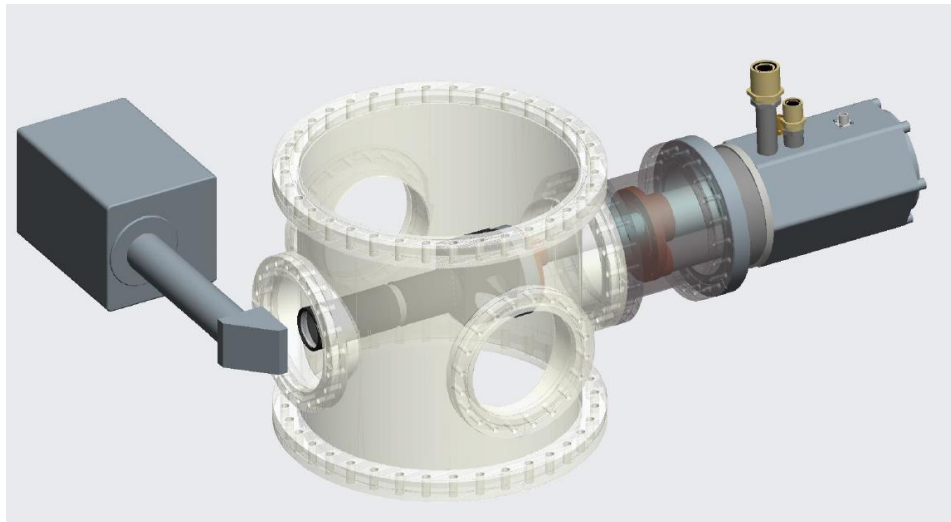

Figure 3.3-1: Open view of test chamber with solar simulator (left) and cryocooler (right). The solar simulator with its attached optics directs radiation into the vacuum chamber where the sample is held. The cryocooler provides cooling of the sample and its enclosure.

The test sample will be hung from a mounting fixture on the mounting platform and exposed to the solar energy beam. Temperature sensors will be mounted in multiple locations to allow for the understanding of any non-solar energy paths into the system. Sensors will also be mounted on the sample itself to allow for a full thermal mapping of the system to understand the coating performance. Due to the mounting orientation of the system, it should be fairly easy

to measure the intensity of the solar simulator on the sample using similar sensors as KSC used, but without having to take the system apart and realign it.

Hardware for this system has been designed and ordered (if not already available at GRC). Testing will commence when the hardware is ready in support of the recently approved Game Changing seedling project. Initially it was planned for checkout testing to occur under the NIAC, however, a delay in the arrival of the custom vacuum chamber has slowed down the build-up and testing.
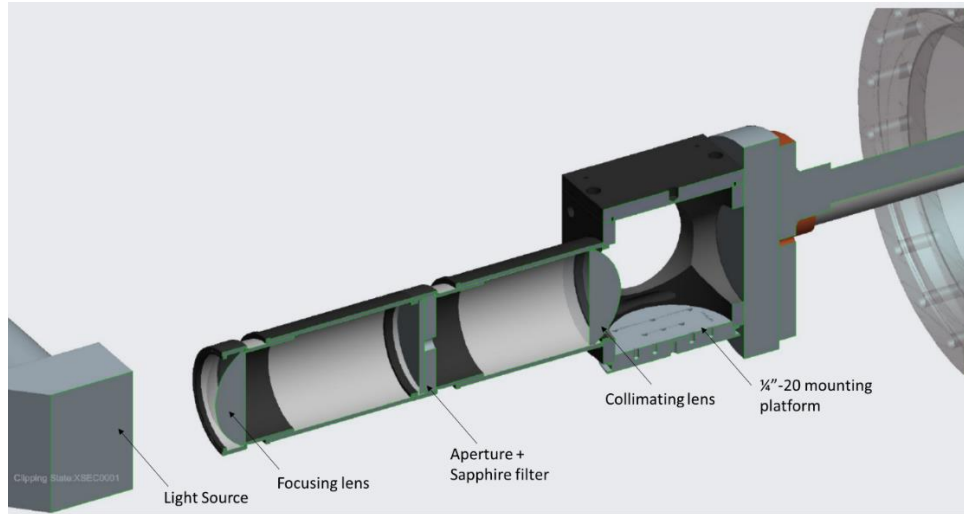
Figure 3.3-2: Cutaway view of items within the vacuum chamber showing a lens that focuses the solar radiation onto an aperture, after which a second lens collimates the radiation. The sample chamber is a cube with access holes located around it in which the sample will be suspended. The cryocooler is attached to these components, chilling them to cryogenic temperatures.

3.4 Thermal Desktop Modeling of the Cryogenic Selective Surface

In order to enable the use of the cryogenic selective surface materials on spacecraft, it is important to demonstrate the capability of thermal software packages to correctly model performance. The thermal vacuum test setup for the 375 nm LED test (see section 3.1) was modeled by GRC using Thermal Desktop (TD), in which thermal analysis was conducted to compare the model results to the data obtained from thermal vacuum testing at KSC. This model includes the sample held in place by a sample holder, which is contained within a vacuum chamber. The LED light source is located directly above the chamber, and is modeled as a sphere with a single node. A heat load of 17 µW (at 375 nm) was outputted from the node through the lens and directed at the sample within the test chamber. The test sample is modeled with wavelength dependent emissivity approximating that of BaF_2 as shown in Figure 3.4-1. The steady-state results from analysis showed the solar white sample temperature to reach 44.84 K (see Figure 3.4-2), which is very similar to the temperature that the sample reached near the end of thermal vacuum testing. The chamber surfaces were also shown to remain at 40 K due to boundary conditions applied to its outer surfaces. This correlation of the model results to the thermal vacuum test data verifies that the cryogenic selective surface was modeled accurately.
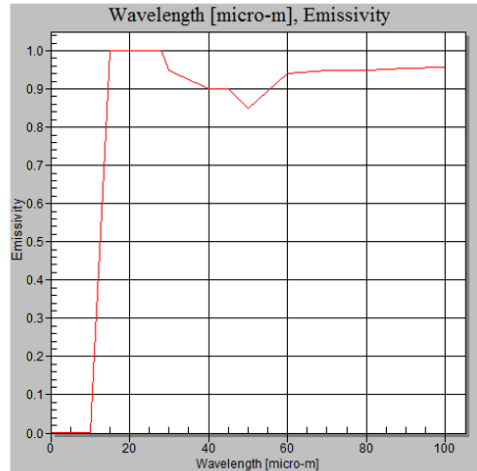
Figure 3.4-1: Wavelength dependent emissivity used in Thermal Desktop to represent BaF$_2$ based cryogenic selective surface, shows the emissivity near zero for short wavelengths and then transitioning to values between 0.8 and 1 for wavelengths longer than 10 microns.
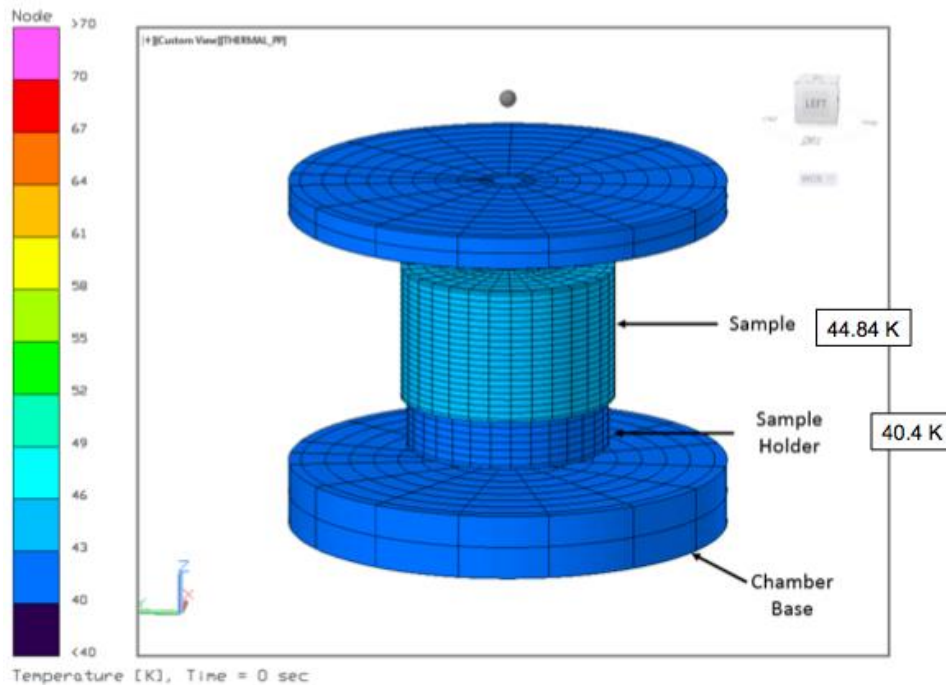

Figure 3.4-2: Steady-state results from the Thermal Desktop model showing the sample reaching a temperature of 44.84K, similar to that seen in testing.

The cryogenic selective surface material was used in another TD model, which consists of an aluminum LOX tank placed on a lunar surface held at a temperature of 220 K. In the model, the LOX tank is coated with solar white and has inner contents of LOX at 90 K. The model also includes a paraboloid that surrounds the tank, which represents the structure that holds the LOX tank in place on the lunar surface. This paraboloid structure was given an effective emissivity of 0.001 since its outer surface is covered with MLI to block the infrared radiation from the lunar surface. The initial model configuration consisted of the tank being located on the pole of the Moon, at a beta angle of $\beta = 90°$. The results from analysis for this configuration showed the outer surface of the paraboloid reaches a maximum of 296.4 K due to the lunar surface (220 K) and sunlight. However, the inner surface of the paraboloid remained cold,

and the LOX tank reached a temperature of about 59.4 K (see Figure 3.4-3). This shows that the MLI-covered paraboloid was effective in preventing heat from reaching its inner contents. Another case was run in which the solar white coating was removed from the LOX tank, which resulted in the tank reaching a higher surface temperature of 81 K. This shows that the solar white coating also had an impact on maintaining the tank and its contents at very low temperatures as desired. This is mostly due to the higher emissivity in the IR range of the cryogenic selective surface because in this configuration, the sphere does not see the sun.

An orbital case was also run for a full lunar orbital period of about 6500 s, which includes the tank being placed at the equator of the Moon. The results from this case showed the LOX tank reached colder temperatures when the tank is at an angle away from the Sun, and warmer temperatures when the tank is at an angle facing the Sun as expected. Further refinement of these configurations and Thermal Desktop model will be performed to better understand the capabilities of Solar White materials in various applications.
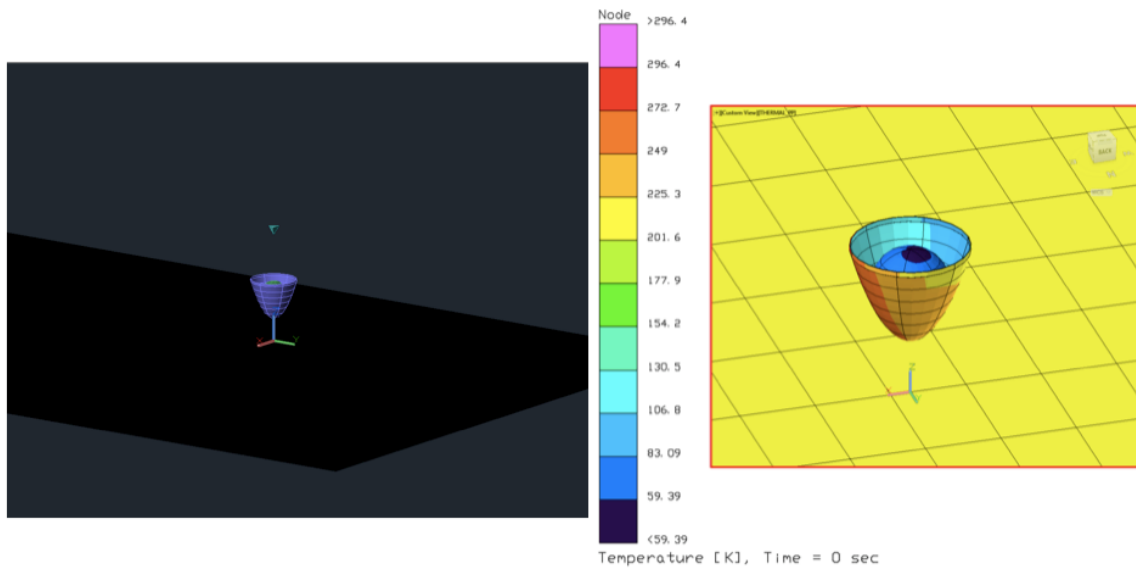

Figure 3.4-3: Lunar Surface Model consisted of a parabola aimed upward that protects a coated LOX sphere from the Moon's infrared radiation. Thermal Desktop modeling shows that the LOX sphere maintains cryogenic temperatures under the given test conditions.

4.   Applications Developed

    4.1   Phase I Results Summary

A key requirement of a NIAC project is to analyze the mission impact of the concept. During our Phase I effort [6], we were asked to determine if our cryogenic selective coating could enable the passive maintenance of liquid oxygen (LOX) on a trip to Mars. We proposed a strawman design, see Figure 4.1-1, and then showed that this would allow LOX to be maintained passively in deep space. We recognized that there were four sources of heat that had to be considered; conductive heat along the support struts, radiant heat from the warm portions of the spacecraft, radiant heat from the Earth/Mars, and solar irradiance. The solar irradiant power contributes an amount of heat that is predicted by the models developed under our Phase I study. We showed that a coated sphere in full sunlight would come to an equilibrium temperature less than 90K, meaning that a LOX tank at 90K would be a net emitter of energy even in full sunlight.
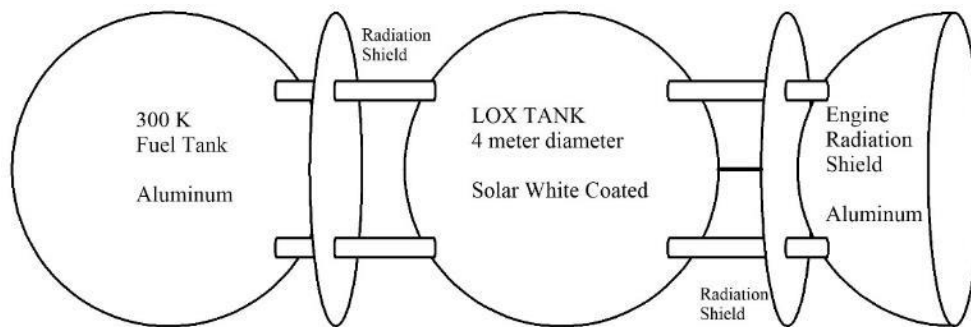
Figure 4.1-1. A strawman sketch of a passively chilled LOX tank on a Mars vehicle. The LOX tank is located between two warm entities, a fuel tank and the engine, and radiation shields are shown protecting the LOX tank from the radiant heat of these warm entities. Also shown are the struts that support the LOX tank.

We then considered the infrared radiation from the warm portions of the spacecraft and from a nearby planet. Our coating is designed to emit in the long wave regions of the spectrum and, as a good emitter; it is a good absorber. Consequently, irradiated infrared radiation will be absorbed and in order to maintain LOX temperatures, most of this must be blocked. We proposed to shield from the spacecraft infrared radiation by adding radiation shields between the LOX tank and the warmer portions of the vehicle as shown in Figure 4.1-1. We also showed that the LOX tank must be shielded from the Earth/Mars infrared radiation, either by maintaining a significant distance or by turning the spacecraft to allow the LOX tank to be shielded from this infrared radiation.

Finally, we considered the conductive heat along the support struts. In current cryogenic spacecraft designs, conductive heat to the cryogenic tanks is the most significant source of heat. We showed, through numerical modelling, that by shielding the struts from infrared radiation (note the infrared radiation shields are placed close to the sources of heat), making them from a low conductivity material (e.g. titanium), and coating them with our cryogenic selective surface, that they would cool to below LOX temperatures along their length before reaching the LOX tank. In other words, with a proper design the struts can be constructed such that they contribute no heat to the LOX tank.

In our Phase I NIAC report we provide the details of this analysis, demonstrating the LOX can be maintained passively on a Mars trip. We also showed that a similar approach can be used to store LOX on the Moon. During our Phase II project, we were approached by the Launch Services Program (LSP) and asked to consider the use of our coating for storing LOX in low earth orbit. We were also approached by the Nuclear Thermal Propulsion (NTP) Program and asked to consider ways to minimize liquid hydrogen boil-off on a Mars trip. Both of these assessments were carried out and are presented below.

4.2 LOX in Low Earth Orbit

The Launch Services Program wants the capability of maintaining liquid oxygen in low earth orbit (200-300 miles). They heard about our new coating and approached us, with funding, asking if there was some way that our new coating could provide this. Our immediate response was negative, since our Phase I work [6] showed that the infrared emission of the Earth is too high to allow our coating to become cold. Our coating is designed to emit long wave radiation, and as a good emitter, it is a good absorber of long wave radiation. The Earth—while not overly warm—occupies a large field of view, so its long-wave irradiance is substantial, preventing our coating from cooling through radiative emission. However, we had only analyzed BaF_2 in this regard and proposed that we redo our analysis to consider whether very broadband materials, such as CsI and KBr might achieve LOX temperatures in low earth orbit. The hope was that CsI and KBr might absorb less of the Earth's radiation since their long wave emission is shifted out to even longer infrared wavelengths.

Upon performing the analysis, we found that neither CsI nor KBr would allow LOX to be passively maintained in low Earth orbit. Both of these materials, even with their shifted absorption spectrum, absorbed too much of the Earth's irradiant power to maintain LOX temperatures. So we met with the LSP team and proposed an alternative architecture. We proposed that the LOX tank be covered with thermal insulation, specifically multi-layer insulation (MLI), over the lower portion of the tank that were exposed to the Earth's radiation, and covered with our cryogenic selective surface over the portion of the tank exposed to only the Sun and deep space, see Figure 4.2-1. The idea is that the MLI would minimize the amount of heat that reached the LOX in the tank, while the cryogenic selective coating would radiate heat away from the tank, even in the presence of the Sun. The LSP team agreed to us performing the analysis on this concept.

The material below summarizes the analysis and presents the conclusions, showing that this approach is feasible. However, a key factor in this analysis is the relative coverage of the tank by MLI and by our coating. We found that more of the tank needed to be covered with our coating than was shaded by the tank itself, so we had to incorporate fins on the tank along the transition between the two coatings. These fins would project out from the tank and provide shielding of the top portion of the tank from the Earth's radiation, allowing a larger are to be covered with our coating.
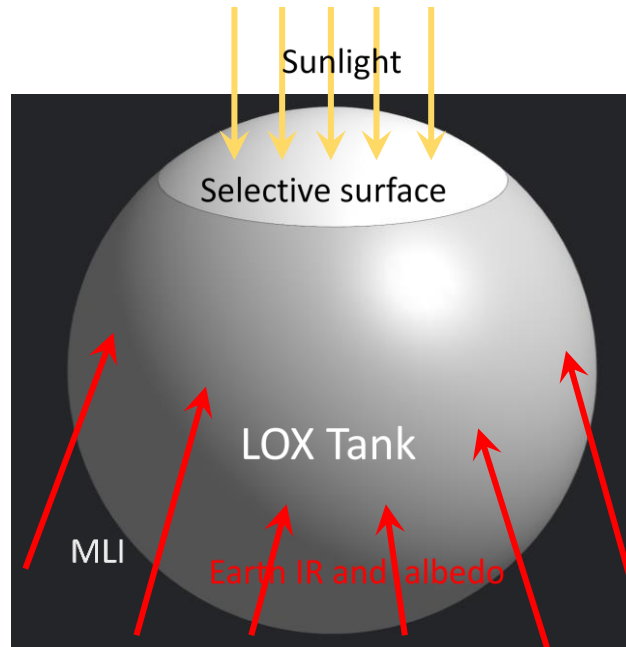
Figure 4.2-1. A sketch of a proposed approach for maintaining liquid oxygen in low earth orbit. A LOX tank has MLI on the lower section to minimize heat from the Earth from getting to the cryogenic liquid. The top of the tank has a cryogenic selective surface on it that minimizes solar absorption and allows excess heat to be radiated away.

4.2.1   Analysis Summary

The tank is modeled as a 1-meter radius sphere made from polished stainless steel. It has MLI on the parts of the sphere that can see infrared radiation from the Earth, while the surface facing away from the Earth is assumed to be coated with our cryogenic selective surface to allow the tank to radiate away heat. However, there needs to be enough cryogenic selective surface area to allow for sufficient cooling of the tank. This requires that the MLI be allowed to flare out normal to the tank. This "fin" is used to block the infrared radiation from the Earth horizon from hitting the cryogenic selective surface. In the analysis, the area covered by cryogenic selective surface was varied along with the corresponding fin size and the steady state temperatures of the MLI and tank were computed.

A blackbody curve doesn't capture the fine details of the solar irradiance spectrum or the absorption bands in Earth's radiance spectrum. Therefore, higher fidelity models are used to represent both these spectra. The 2000 ASTM standard extraterrestrial reference spectrum, E-490-00, used in this analysis is shown in Figure 4.2.1-1 for air mass zero solar spectral irradiance [13]. It is based on data from satellites, Space Shuttle missions, and other high-altitude data. The solar irradiance spectra are used to compute the direct solar heat load on the tank configuration and the load from the Earth scattered sunlight known as the albedo. The Earth's radiance is computed with the Monochromatic Radiative Transfer Algorithm (MRTA) developed by Kratz [14] and provided to us by Dr. Martin Mlynczak of NASA's Langley Research Center (see Figure 4.2.1-2). We have selected the mid-latitude summer radiance spectra as a conservative model. The Earth radiance spectra is needed to determine the power absorbed by a MLI shield from the Earth's infrared (IR) radiation.
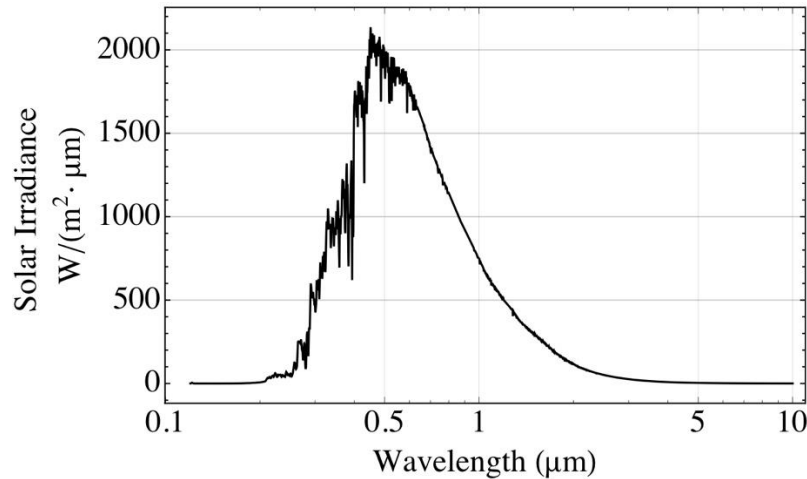
Figure 4.2.1-1: Plot showing the 2000 ASTM Standard Extraterrestrial Spectrum Reference E-490-00 corresponding to the solar irradiance density at 1 AU as a function of wavelength.
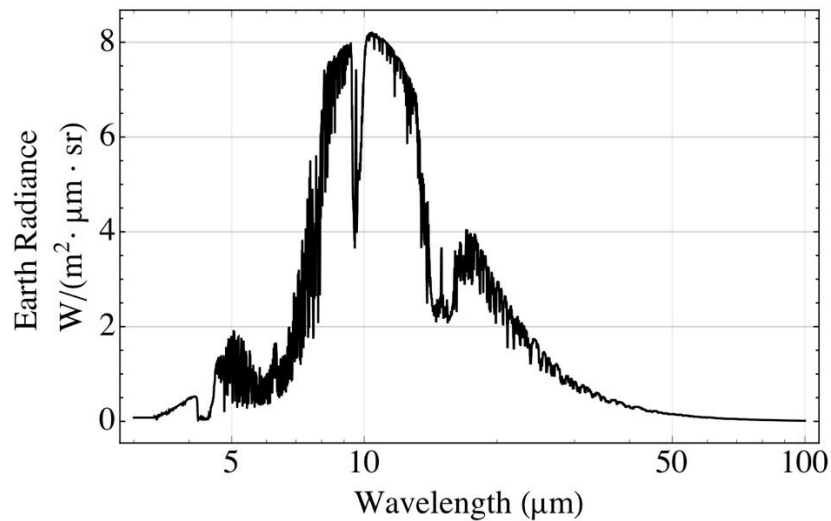

Figure 4.2.1-2. Plot showing the Earth radiance spectrum for mid-latitude summer as a function of wavelength.

In order to carry out computations, some assumptions are needed regarding the geometry and the radiative properties of the materials. The MLI shield is assumed to consist of one or more layers of silver backed polymer film (second surface mirror) that emit in the IR above 2.5 μm. The film is transparent in the visible and the silver is used to reflect the solar spectrum, but some absorption still occurs. Typical values given in Sheldahl's Red Book [15], show that each MLI layer would have an emissivity of about 0.85 and an absorptivity of 0.10 on the plastic (Earth facing) side of the MLI. The silver side has a low emissivity of around 0.02, sending less energy in the direction of the tank. The cryogenic selective surface coating is the 5 mm thick barium fluoride coating described in our NIAC Phase I report [6]. Prior cryogenic selective surface modeling shows that the BaF$_2$ coating absorbs about 1 W/m^2, has an emissivity of 0.853 at a temperature of 93 K and emits above 12 μm. The tank is made from polished stainless steel, which has an emissivity of approximately 0.04 at cryogenic temperatures. A final key assumption is that the time constant for the tank to respond to a change in power load is much longer than the orbital period around the Earth. This means that the day/night cycles will average out and the Sun loads will only be present half of the time.

The MLI shield on our tank will see three main sources of radiated power: the IR from the Earth, the albedo, and the sunlight that directly strikes the MLI. The IR from the Earth can be modelled by taking note of the field of view from the tank's perspective. We have selected to model the Earth's emission as a spherical dish shaped emitter that is located at a distance equivalent to the altitude of our tank. The total radiated Earth power absorbed by the MLI can be found by integrating the power that reaches the tank from each differential element of the Earth's angular surface and accounting for the change in absorption of the MLI at 2.5 microns.

The power absorbed from the Earth's albedo uses a similar computation, but adjustments must be made to the solar spectrum. The solar spectrum is in terms of irradiance and the rays are all parallel coming from the Sun. However, when they are scattered by the Earth, assuming the resulting scattering is Lambertian, the power absorbed by the LOX tank is found by integrating over the angular extent of the Earth. Much of the solar spectrum is at wavelengths shorter than 2.5 μm, so most of the Sun's energy will be reflected by the MLI shield. However, there is an infrared tail that will be absorbed.

The final heat load on the MLI is from direct sunlight reaching it. As a conservative approximation, the worst-case direct sunlight exposure will occur when the sun is along the Earth horizon, illuminating exactly half of the tank and due to the fins, only reaches the MLI. This is a worst case because the MLI absorbs more solar power than the cryogenic selective coating. We also assume the Sun is only present half of the time as the tank orbits the Earth.

Now, calculate the power radiated by the MLI covering the tank and fins. The MLI radiates power away from the tank and allows a small amount of power to make it through to the tank. By equating the emitted and the absorbed power by the MLI, a power balance equation for the equilibrium temperature can be found and from this, depending on the specifics of the MLI, the amount of heat reaching the LOX can be determined. This absorbed power for the equation consists of the power from the Earth, the sun's albedo, and the direct sunlight hitting the MLI. The power emitted consists of the MLI radiation, the fin radiation, and the transfer to the tank through the MLI.

To complete the analysis, a second power balance equation is needed containing the power entering and leaving the tank through the cryogenic selective surface and through the MLI. The power emitted by the cryogenic selective surface is given by its emissivity times its area. The power absorbed by the cryogenic selective surface is given, from our prior work, as 1 W/m^2 of direct solar normal area times a ½ day/night factor. So for this second equation, the power absorbed is the power that makes it through the cryogenic selective surface plus the power radiated by the fin back at the selective surface, plus the power transferred through the MLI. The emitted term is the power radiated away through the selective surface. To model the transfer through the MLI, it is common practice to lump the heat transfer mechanisms together and treat it as a conductive heat source [16, 17]. However, these models don't capture the non-linear behavior of radiative heat transfer. A more accurate MLI model was provided by Wesley Johnson [18] of NASA's Glenn Research Center. This model provides the conducted power into the LOX tank as a function of the temperature of the outer layer of MLI, the tank temperature, the number of layers of the MLI, the layer density, and the pressure, which is assumed to be vacuum.

4.2.2   Results

Figures 4.2.2-1 and 4.2.2-2 show the steady state LOX tank temperatures as a function of fin length and MLI layer count for tank altitudes of 200 and 300 miles, respectively. These plots show that it is possible to achieve steady state temperatures below 100 K with only three layers of MLI, but large fin sizes are required. Use of a 30-layer MLI achieves steady state temperatures below 90 K for fin sizes as small as 2.5 cm (this assumes a 1 meter radius tank). Since 30 layer MLI is readily available for space application, this analysis demonstrates one potential architecture where LOX could be passively maintained in low earth orbit.
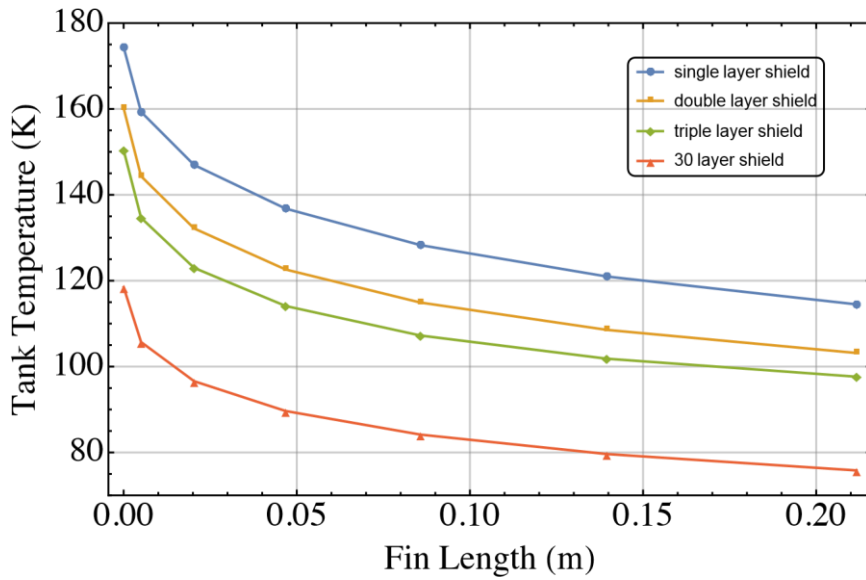
Figure 4.2.2-1: A plot showing the steady state tank temperatures achieved for an altitude of 200 miles above the Earth as a function of fin length and for four different MLI insulations; one layer, two layers, three layers and 30 layers. Liquid oxygen temperatures are only achieved using 30 layer MLI and with fins at least 0.05 meters in length.
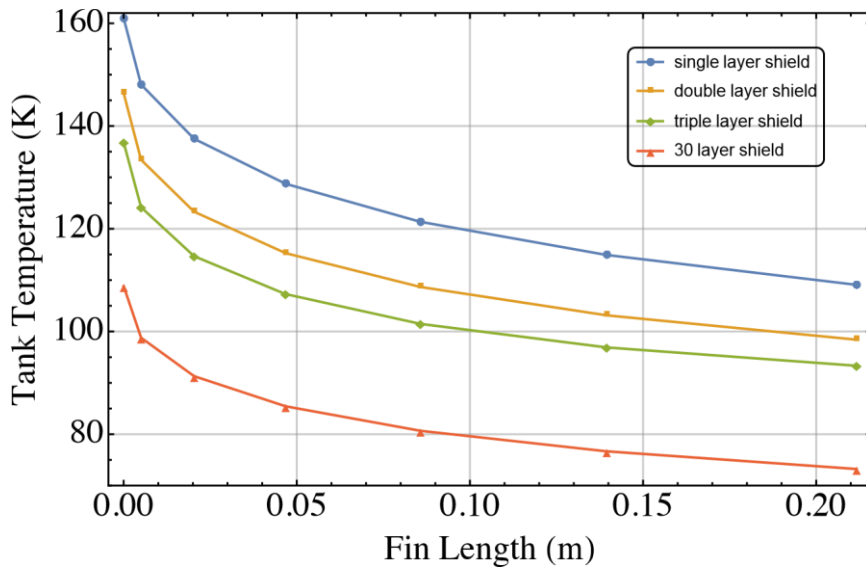

Figure 4.2.2-2: A plot showing the steady state tank temperatures achieved for an altitude of 300 miles above the Earth as a function of fin length and for four different MLI insulations; one layer, two layers, three layers and 30 layers. Liquid oxygen temperatures are only achieved using 30 layer MLI and with fins at least 0.02 meters in length.

4.3 Enhanced Multi-Layer Insulation

The current design for the Nuclear Thermal Propulsion (NTP) LH$_2$ tank insulation is a two-layer system composed of foam covered with multilayer insulation (MLI). This combination yields impressively low thermal conductivity, but the outer surface may absorb significant solar radiation, resulting in an outer surface temperature that is higher than desirable. By spraying the outer surface of the MLI with a coating that reflects a large portion of the Sun's irradiance, this temperature can be reduced, resulting in less conductive heat transmission to the LH$_2$. This section briefly summarizes the theoretical benefit of such a coating and then describes the accomplishments made towards developing such a coating.

4.3.1 Potential Benefit

If a surface is facing the Sun at 1 astronomical unit (AU), the total broadband solar irradiance is about 1366 W/m^2 expressed as I_S. If the surface absorbs some fraction of that solar irradiance, α, the total absorbed power density is αI_S. The surface then becomes warm and emits power in the infrared with emittance, ε. The power density emitted is given by the Stefan Boltzmann Law as $\sigma \varepsilon T^4$, i.e. the product of the Stefan-Boltzmann constant (5.67x10^{-8} W/(m^2-K^4)) times the emissivity times the temperature of the surface raised to the fourth power; this result assumes that the emittance is constant across the emitted spectral region. If the emittance is constant across all wavelengths from the ultraviolet through to the long wave infrared, i.e. a grey-body, then the absorption equals the emission for all wavelengths, $\alpha = \varepsilon$. If this is the case, then equating power absorbed to power emitted, i.e., $I_S = \sigma T^4$, yields a surface temperature of 394 K, or about 120 °C (the Moon is a grey-body and has a maximal surface temperature of 127 °C, substantiating this result).

Now consider multi-layer insulation (MLI). Typically, the outer layer of MLI is silver or aluminum, which absorbs the ultraviolet power from the Sun and has difficulty emitting in the infrared (metals are not grey bodies), yielding excessive temperatures (over 500 K). So assume the MLI has a layer of Teflon™ covering the outer layer of silver, yielding a reflector having solar absorptivity of about 0.09 and emissivity in the infrared of 0.9. This allows most of the Sun's power to pass through the Teflon™ and reflect off the silver, yet the Teflon™ is black in the infrared, allowing efficient emission of thermal power. A plate coated with this would have a surface temperature of about 220 K, (obtained from the Stefan Boltzmann Law, $0.09 I_S = 0.9 \sigma T^4$) which is cold, but still leaves a 200 degree difference between the outside of the tank and the inside.

The performance limitation of Teflon™ on silver, a so-called second surface mirror, is ultraviolet absorption by both the Teflon™ and silver. A coating, other than Teflon™, is needed that will reflect most of the short-wave radiation emitted by the Sun, will transmit mid-wave radiation that can be reflected by the silver, yet will turn black in the far-infrared, allowing heat to be radiated away. If such a coating, placed on silver, reflected 99% of the Sun's power and still had a 0.9 long-wave emissivity, then it would have a surface temperature of 128 K (obtained by solving the Stefan Boltzmann Law, $0.01 I_S = 0.9 \sigma T^4$). This results in roughly half the temperature difference across the thermal insulation, yielding about half the conducted heat flow.

4.3.2 The Concept

Work funded by the NASA Innovative Advanced Concepts (NIAC) program at KSC and GRC has resulted in a new, potentially breakthrough, solar reflector based on particle scattering. The concept, which describes why snow and clouds are white, is that small particles of non-absorbing material scatter the light that hits them. Since they are non-absorbing, the light can only bounce between the particles and eventually makes its way out, preferentially to the front side for sufficiently thick materials. The challenges are to select materials that are non-absorbing over most of the

Sun's spectrum, that can form a mechanically stable coating, and that have particles and void fractions in desirable ranges. The NIAC funded work found several materials that meet these criteria, two of which are yttrium oxide (Y_2O_3) and potassium bromide (KBr).

Yttrium oxide is available as a fine powder (100 nm diameter, which is smaller than desirable) that can be pressed into molds and sintered (at about 1000 °C) to create rigid "tiles". A 3 mm thick tile with moderate void fraction (about 60%) blocks essentially all visible light. Y_2O_3 has high index, so it is an efficient scatterer, and is hydrophobic, so water retention is not an issue. However, it does absorb a small amount of solar ultraviolet radiation (below 235 nm). It transitions from being transparent to black in the 12-14 micron region of the spectrum, becoming a good emitter of long wave radiation. Current work with this material is promising, but it cannot be sintered onto MLI without melting the MLI. Potassium bromide is transparent over a very broad spectral range, from 210 nm to 20 microns. However, it dissolves readily in water, making its use questionable as a fine powder with large surface area in humid environments.

Both materials have issues, but used in combination they achieve a potentially useful type of "white" paint. Start by dissolving KBr in water and then add powdered Y_2O_3 to make a white slurry. This can be applied to a surface and allowed to dry, causing the KBr to come out of solution and recrystallize as a glue to hold the Y_2O_3 particles in place and to hold the resulting white coating to the application surface. The resultant structure is nearly identical in structure to commercial white paint where transparent glue holds titanium dioxide (TiO_2) particles in place. Figure 4.3.2-1 shows an airbrush used to spray the slurry of Y_2O_3 mixed in KBr laden water and also shows three sapphire windows sprayed with various thickness of this novel paint; 4 spray layers on the left sample, 8 spray layers on the middle one, and 12 spray layers on the right one.
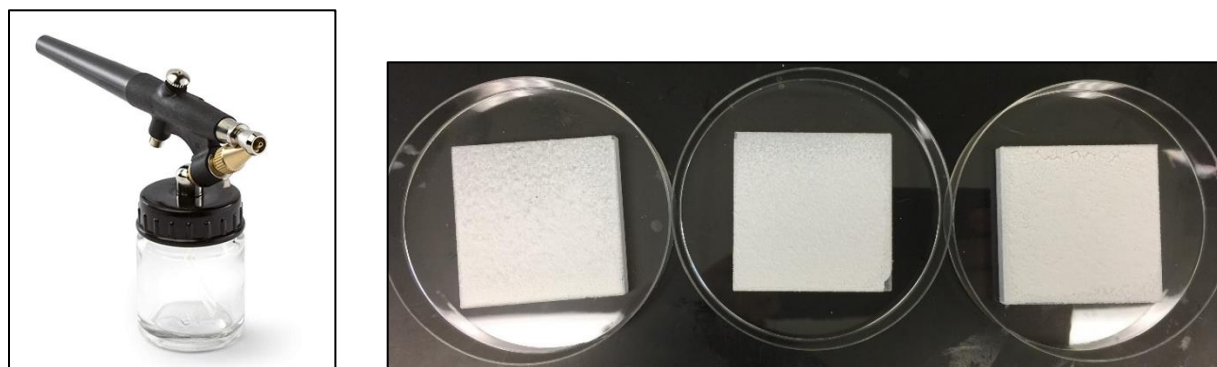
Figure 4.3.2-1. An airbrush and sapphire windows coated with different thickness of KBr/Y_2O_3. 4 Layers (Left), 8 Layers (Middle), and 12 Layers (Right) showing that the coating becomes thicker and whiter with more sprayed on layers.

The reflectance of the three, coated, sapphire windows was measured with a reflectance spectrometer and compared to Spectralon, a NIST standard for reflectance. The results are shown in Figure 4.3.2-2 for a spectral region from the ultraviolet through the near infrared. In the ultraviolet, the coating reflects better than Spectralon, a promising result, but the reflectivity drops rapidly with wavelength. This is likely a result of Mie/Rayleigh scattering where light scatters optimally from particles when the wavelength matches the circumference (about 300 nm in this case), and then drops as one over wavelength to the fourth power.
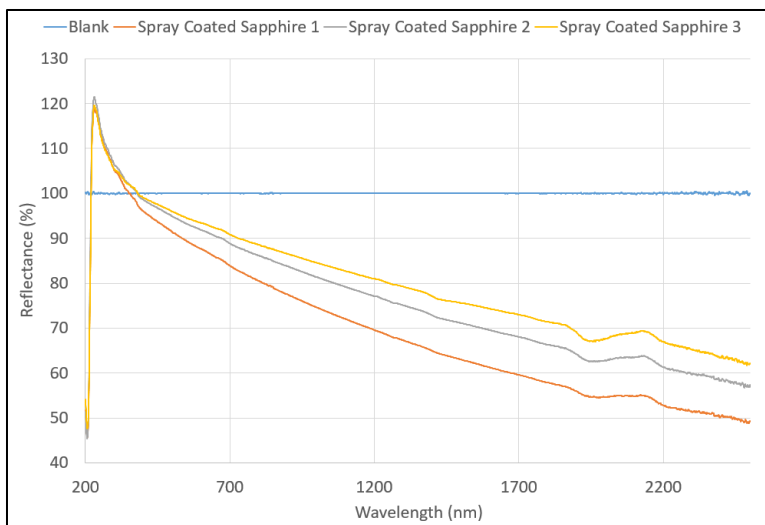
Figure 4.3.2-2. Reflectance spectra of the three sprayed sapphire windows compared to Spectralon from 200 to 2400 nm wavelength. The reflectance spectra are the same in the ultraviolet showing better reflectance than Spectralon. All three plots then decrease with increasing wavelength, with the thicker coatings having more reflectance, eventually having reflectances between 50 and 65 % that of Spectralon at 2400 nm.

4.3.3   Refinements of the Spray-on-Coating

A variety of mixture ratios of KBr to Y_2O_3 were prepared and tested. They were applied with brushes to a variety of flexible surfaces and examined for uniformity, optical performance, and adherence (cracking and flaking). Surprisingly, the coatings, which were between 1 and 4 thousands of an inch thick, had good adherence. The substrate materials could be flexed and the coatings, for most cases, stayed in place without significant damage. Figure 4.3.2-3 shows a metallized polyester film that has had the material applied with a brush, resulting in an uneven coating. It was found that the optimal ratios for KBr, Y_2O_3, and H_2O were 20%, 20%, and 60%, respectively. Figure 3 also shows a piece of silver-coated Kapton™ that has been coated with this optimal ratio of KBr/Y_2O_3 using an airbrush, resulting in a more even distribution of material. However, a careful examination of the coating shows that it is still uneven and that small cracks still appear in time.

In an attempt to improve the uniformity of the coating and to remove the cracking, some methanol was mixed with the water-KBr mixture to improve the wetting of the slurry. This did improve the coating. Figure 4.3.2-4 shows a piece of silver-coated Kapton™ before and after air-brush spraying of the coating with methanol added. Figure 4.3.2-5 shows the reflectance curve of the silver-coated Kapton™ before and after application of the KBr/Y_2O_3 coating. Recall that silver has a very strong ultraviolet absorption at about 300 nm and this appears in the reflection curve (note that the spectrometer may have an offset in the data as indicated by the step at 850 nm where the device has a grating change). After coating the sample, the reflectivity in the ultraviolet has increased substantially and the silver now reflects the longer wave radiation that went through the sapphire coating. Quantifying the improvement is difficult due to the spectrometer limitations, but a factor of five times better reflectivity in the ultraviolet portion of the spectrum seems justifiable.
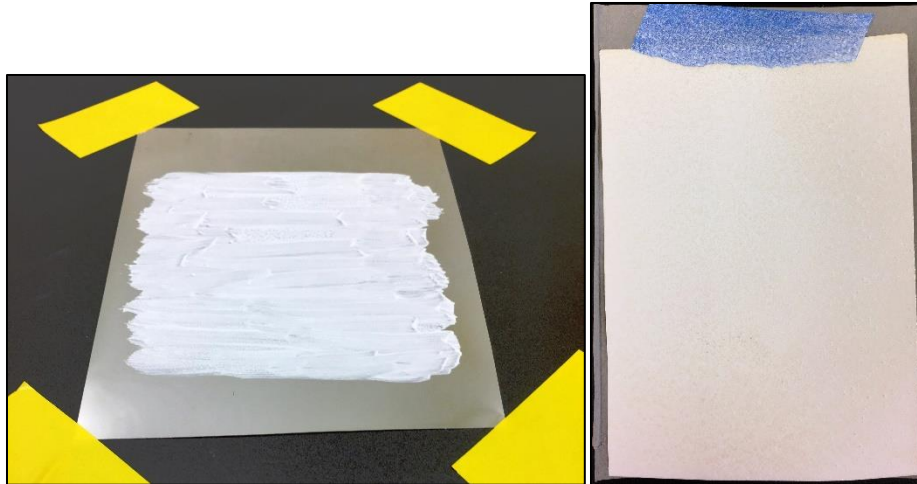
Figure 4.3.2-3. A metallized polyester film brushed with the KBr/Y$_2$O$_3$ slurry and silver-coated Kapton™-HN film coated with the KBr/Y$_2$O$_3$ slurry using an airbrush. Brush application yields an uneven coating after drying. The airbrush yields a more uniform coating, but is not ideal.

Figure 4.3.2-4. Silver-coated Kapton™-HN before and after coating with an airbrush using the methanol mixture. The silver-coated Kapton is highly reflective and after coating, is white and highly diffuse.

Figure 4.3.2-6 shows a scanning electron microscope (SEM) image of the spray coated, silver-coated, Kapton™ film. The KBr has formed into continuous material that holds the Y$_2$O$_3$ particles in place.

The coating was applied to both aluminum and silver coated flexible sheets and was found to have better adherence to silver than aluminum, but in either case, no chemical induced damage to the underlying material was seen when the coating was removed. However, this was not the case for other metals. Test plates of 3003 Aluminum, 6061 Aluminum, and 7075 Aluminum were coated and then had the coating removed. In all three cases, corrosion was apparent. Since no corrosion was seen on the pure aluminum samples it is believed that the coating, while in liquid form, is interacting with other metals present in these aluminum alloys. Al-2219-T81 was also tested and showed corrosion, but when the methanol was replaced with ethanol it did not show corrosion. The replacement of methanol with ethanol was done to reduce the toxicity of the process, so this reduction in corrosion was a positive byproduct of that change. Test plates of 304L and 316 Stainless Steel were coated and no corrosion was seen after removal of the coating. Figure 4.3.2-7 shows the 304L test plate before and after being coated. Also shown is the before and after reflectance data, showing the dramatic improvement in reflectivity achieved by applying this coating.
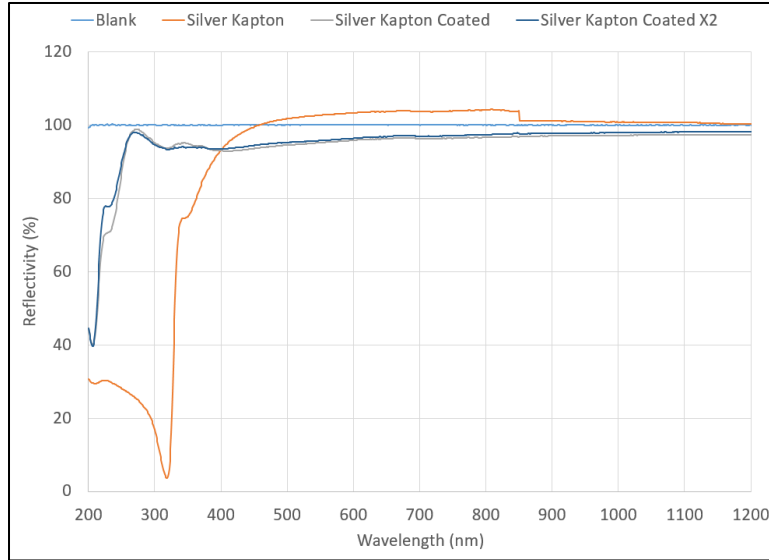
Figure 4.3.2-5. Reflectance spectra for silver-coated Kapton™ and spray-coated silver-coated Kapton™ versus wavelength from 200 nm to 1200 nm. Silver strongly absorbs radiation in the ultraviolet which is significantly reduced applying the coating.
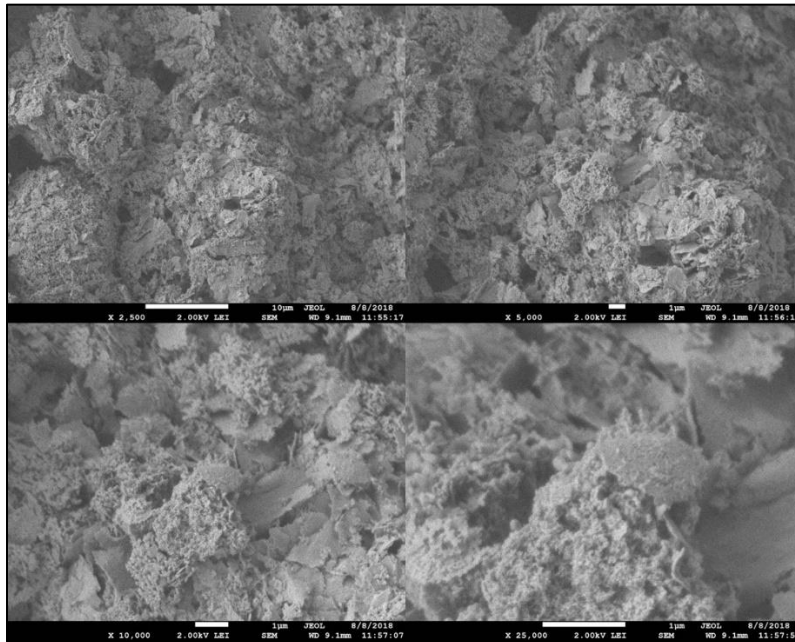

Figure 4.3.2-6. These SEM images of spray-coated silver-coated Kapton™-HN film show the KBr has formed into continuous sheets that hold the Y_2O_3 particles in place.
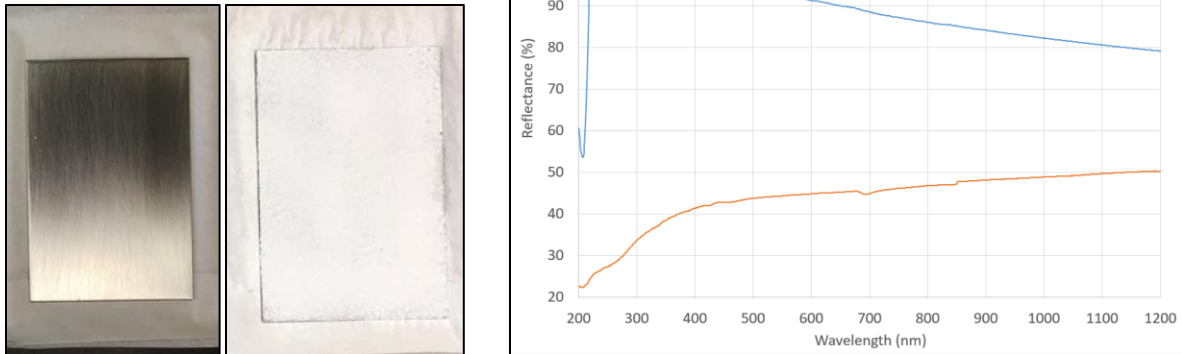
Figure 4.3.2-7. An uncoated and coated 304L stainless steel test plate along with reflectance data showing that the reflectance is much higher after spraying the steel with the KBr/Y$_2$O$_3$ coating.

5.   Project Timeline (indicating co-funding, interest, and follow-on work)

       This section of the report provides a timeline for the work in order to highlight co-funding and outside interest. It also shows our attempts to publicize the work and to obtain follow-on, post-NIAC, funding.

1. May 2015:   Our Phase I NIAC entitled Cryogenic Selective Surfaces started.

2. July 2015:   We discovered a promising new cryogenic selective surface.

3. August 2015:   A provisional patent was sent to the US Patent Office.

4. October 2015:   Our first NIAC Symposium (Seattle).

5. December 2015:   Gave a KSC presentation to Steve Jurczyk and the Launch Service Program.

6. January 2016:   The LSP program provided contractor dollars and KSC provided NASA labor to continue the work after the Phase I had ended.

7. February 2016:   Submitted our Phase I final report and a Phase II proposal to continue the work.

8. March 2016:   Our Optics Letter publication appeared in print.

9. May 2016:   Internal KSC contractor funding was obtained to support this project.

10. May 2016:   Our Phase II NIAC proposal was accepted. We now had a partner at the Glenn Research Center.

11. August 2016:   Our second NIAC Symposium (Rayleigh).

12. September 2016: A patent application was submitted.

13. October 2016:   We received a small Game Changing seedling project to provide NASA labor (0.5 FTE).

14. January 2017:   The LSP provided funding to study LOX storage in low earth orbit.

15. June 2017:   We successfully passed our mid-term review.

16. August 2017:   A second provisional patent was sent to the US Patent Office.

17. September 2017: Our third NIAC Symposium (Denver). After the symposium both Northrop-Grumman and Lockheed Martin thermal engineers contacted us and requested further information on our work. JPL also showed significant interest and a telecom presentation was arranged.

18. October 2017:   A Future-In-Space-Operations (FISO) seminar was given on our new coating.

19. October 2017:   We received funding from the Nuclear Thermal Propulsion Program to determine if our coating could help maintain liquid hydrogen.

20. November 2017: We sent a sample of our BaF_2 rigid material to Goddard for inclusion on a Materials International Space Station Experiment (MISSE) X , low earth orbit experiment [described in 10]. We now had a potential partner at Goddard Space Flight Center.

21. December 2017: Our paper in the Journal of Spacecraft and Rockets was published.

22. December 2017: The LSP program provided more funding to support this work.

23. April 2018: Submitted a proposal for Game Changing Funding (FY2020 start).

24. May 2018: Attended NASA "Tech Day on the Hill" event to showcase our work.

25. May 2018: Blue Origin requests information on our coating and offered to help "fast track it".

26. June 2018: At the request of the Science Mission Directorate, a brown bag presentation was given at NASA Headquarters.

27. August 2018: We presented our NIAC funded work to the new NASA administrator during a KSC visit.

28. August 2018: A second patent application was submitted to the US Patent Office.

29. August 2018: We received approval for a Game Changing Seedling project to run in FY19. The Glenn Research Center will run this project and will develop a new version of the deep space simulator.

30. September 2018: We began negotiations with a small satellite group at AMES to develop a cube sat to test the performance of our coating in low earth orbit.

31. September 2018: The Nuclear Thermal Propulsion Program is planning to continue to develop and test our new spray-on-coating in order to improve the performance of multi-layer-insulation on the liquid hydrogen tanks.

32. October 2018: The LSP program has approved funding for us to demonstrate superconductor operation in a simulated deep space environment.

33. October 2018: A third provisional patent will be submitted to the US Patent Office.

34. October 2018: Our Game Changing project starts and we plan to continue simulated deep space environment testing and coating development. Our partner at GRC will start higher fidelity simulated deep space environment testing this fall.

6.   Conclusions and Future Work

Substantial effort has been expended in the development, testing, and application of a cryogenic selective surface. Development and testing has resulted in rigid particle scattering materials composed of barium fluoride, yttrium oxide, and a composite of yttrium oxide and potassium bromide that all have, to within our ability to test, the proper broadband optical properties to construct a cryogenic selective surface. Barium fluoride is the most developed and has the broadest optical spectrum. We suspected that it had water retention issues, but recent testing has started to indicate that this may not be an issue. Moderately strong tiles can be made that are about 5-6 mm thick that have very little optical transmittance and very good reflectivity. Yttrium oxide's optical properties are still somewhat unclear, but due to its high index, can effectively block visible radiation with a sintered tile less than 3 mm thick. Purchased samples indicate that tiles of yttrium oxide can be made to high strength and yet retain good optical scattering. So, while yttrium oxide may absorb more solar radiation that barium fluoride, its high index, hydrophobic nature, and potential for increased strength may make it a preferable choice. Finally, the composite yttrium oxide and potassium bromide has been demonstrated as a spray-on coating. It has reasonable uniformity and, for a thin coating, good optical properties.

Barium fluoride sintered tiles have been nearly optimized, with good understanding of the particle size, water issues, pressures, and sintering temperature profile required to achieve a nearly optimal tile. However, yttrium oxide has not yet been optimized and more work is needed to achieve a best compromise between optical performance and strength. Also, additional work is needed to determine if silver can be deposited onto these tiles, or if silver, or some other highly reflective metal, can be attached in some other manner. Finally, the spray-on coating is an exciting development and needs adherence testing, better uniformity, and more application development.

Testing in a deep space simulated environment with a low-fidelity Xenon lamp has shown just over 1% absorption of simulated solar irradiance, which is much better than the state-of-the-art 6-8%. However, all ground-based testing is suspect since it is very difficult to simulate the Sun's spectra, especially in the ultraviolet and longer wave infrared regions of the spectrum. Even so, higher fidelity testing will soon occur at GRC and further testing will occur at KSC in an attempt to refine the test conditions and better determine the actual absorption of our cryogenic selective surface.

In our Phase I effort we showed that this coating could enable passive LOX maintenance on a trip to Mars and we extended that work to include a LOX depot on the Moon's surface. Under our Phase 2 effort we developed a concept to allow LOX to be maintained in low earth orbit and we developed a method for improving the performance of multi-layer insulation to better maintain liquid hydrogen on a trip to Mars. This work will continue into FY19 under nuclear thermal propulsion program funding. The Launch Service Program (LSP) is funding us in FY19 to demonstrate that we can operate a superconductor in a solar illuminated deep space environment using our coating. Also, the LSP and a group at AMES have started a cube-sat effort to get a sample of our coating into low Earth orbit so it can be tested in a more appropriate environment. Finally, there is an effort to propose this new coating as a lunar payload that might be carried on a lunar vehicle in the next few years.

7. Acknowledgements

8. REFERENCES

1. C.G. Granqvist, "Radiative heating and cooling with spectrally selective surfaces," *Applied Optics* **20**(15):2606−2615 (Aug 1, 1981) (A short review article with 349 references).

2. J.H. Henninger, "Solar Absorptance and Thermal Emittance of Some Common Spacecraft Thermal-Control Coatings," NASA Reference Publication 1121 (Apr 1984).

3. D.F. Hall and A.A. Fote, "Thermal Control Coatings Performance at Near Geosynchronous Altitude," *J. of Thermophysics and Heat Transfer* **6**(4):665−671 (Oct−Dec 1992).

4. "Spacecraft Thermal Control and Conductive Paints/Coatings and Services Catalog," AZ Technology, Huntsville, AL (Jan 2008).

5. Qioptiq site on space technology-link at bottom to their solar reflectors. http://www.qioptiq.com/space.html

6. Youngquist, Robert C., and Mark A. Nurge. "Cryogenic selective surfaces", NIAC Phase I Final Report. February 2016.

7. Youngquist, Robert C., and Mark A. Nurge. "Achieving cryogenic temperatures in deep space using a coating." *Optics letters* 41, no. 6 (2016): 1086-1089.

8. R.R. Hibbard, "Equilibrium Temperatures of Ideal Spectrally Selective Surfaces," *Solar Energy* **5**(4):129−132 (Oct−Dec 1961).

9. Grum, F., and G. W. Luckey. "Optical sphere paint and a working standard of reflectance." *Applied Optics* 7, no. 11 (1968): 2289-2294.

10. Youngquist, Robert C., and Mark A. Nurge. "Solar Surfing", NIAC Phase I Final Report. April 2018.

11. Youngquist, Robert C., Mark A. Nurge, Wesley L. Johnson, Tracy L. Gibson, and Jan M. Surma. "Cryogenic Deep Space Thermal Control Coating." *Journal of Spacecraft and Rockets* 55, no. 3 (2017): 622-631.

12. Hogan, Patrick, Todd Stefanik, Charles Willingham, and Richard Gentilman. *Transparent yttria for IR windows and domes-past and present*. RAYTHEON INTEGRATED DEFENSE SYSTEMS ANDOVER MA, 2004.

13. "A Comparison of ASTM E-490 and Wehrli 1985", National Renewable Energy Laboratory (NREL), Renewable Resource Data Center, URL:http://rredc.nrel.gov/solar/spectra/am0/E490_00a_AM0.xls[retrieved 24 July 2017]

14. Kratz, D. P., "The sensitivity of Radiative Transfer Calculations to the Changes in the HITRAN Database from 1982 to 2004," *J. Quant. Spectrosc. Radiat. Transfer*, 2008, Vol. 109, pp. 1060-1080. doi:10.1016/j.jqsrt.2007.10.010.

15. "The Red Book," Sheldahl, A Multitek Brand, URL:http://www.sheldahl.com/documents/RedBook.pdf[retrieved 24 July 2017]

16. Flynn, T. M, "Cryogenic Engineering," Marcel Dekker Inc., New York, 1997, pp. 395-421. doi:10.1002/cite.330700520.

17. Barron, R. F. "Cryogenic Systems," Oxford University Press, New York, 2nd ed., 1985, pp. 396-399

18. Johnson, Wesley, and James Fesmire. "Thermal performance of low layer density multilayer insulation using liquid nitrogen." In *AIP Conference Proceedings*, vol. 1434, no. 1, pp. 39-46. AIP, 2012.